Applying Neutron Star Atmosphere Models to Light Curves from Hot Spots

by

Kuo I Tung

A thesis submitted in partial fulfillment of the requirements for the degree of

Master of Science

Department of Physics
University of Alberta

Abstract

Neutron stars provide the key to understanding the equation of state at the highest pressure and density. Constraining the mass-radius relation of neutron stars will provide opportunities to test the currently conflicting candidates for the equation of state. Next generation instruments, such as the recently launched X-ray telescope NICER, will provide high timing and spectral resolution observations. Its primary objective is to to constrain the properties of nearby isolated millisecond pulsars such as PSR J0437-4715. We present new additions to the routines of the hot spot modelling program at the University of Alberta, with emphasis on adapting neutron star atmosphere models, realistic background sources, and processing of the signals from detected neutron stars to the program. The program will be a valuable tool, useful for interpreting NICER's observations of millisecond pulsars.

Preface

This thesis is original work by Kuo I Tung. This thesis work covers the modifications made to the hot spot modelling program at the University of Alberta. We obtained estimates on the properties of PSR J0437-4715 and neutron star atmosphere models from the NICER science team. Some results have been used to verify the hot spot modelling program of the NICER science team.

"Mental health? What's that?"

Erika Lloyd on graduate students finishing the theses.

Acknowledgements

The thesis project is completed because of the support I received from many members of the community. I would like to **thank** my kind supervisor **Sharon Morsink** for all the guidance, both in academia and in outreach, during my time at the University of Alberta; group members of the Astro-ph group, in particular faculty members **Craig Heinke, Gregory Sivakoff**, graduate students **Arash Bahramian, Eric Koch, Reuben Gazer, Alex Tetarenko**, and **Bailey Tetarenko** for advice on the science; **NICER science team** for the opportunity to contribute; friends at **University of Alberta Taiwanese Association** and **Graduate Physics Student Association**; **Wytze Brouwer** for mentoring my progress in the Graduate Teaching and Learning Program; **Faculty of Graduate Studies and Research** for funding the trip to CRAQ summer school and the GTL program for teaching assistantship; and **Snow Valley** for the chance to teach snowboarding outside of the academic life.

The past two years have been a soul-searching experience for me. The University of Alberta provides great support in the form of counselling services at SUB and at Homewood Health. In addition to the resources, I would like to thank everyone in the community for providing a friendly and supportive environment.

Contents

1 Introduction **1**

1.1 Neutron Star Basics 1

1.2 Neutron Star emission mechanism: radio, X-ray binaries, accretion, and rotation 2

1.3 Light Curve of the Neutron Star Hot Spots 4

1.4 Millisecond Pulsar and the Need for a Neutron Star Atmosphere Model 5

1.5 Brief Overview on the Neutron Star Atmospheric Models 6

1.6 Next Generation Instruments: *Astrosat* and *NICER* 12

1.7 Organization of the Thesis 12

2 Mathematical Background **14**

2.1 Radiation Basics 14

2.2 Numerical Formulas for Interpolation and Integration 18

2.2.1 Interpolation 18

2.2.2 Integration 21

2.3 NS Hot Spot Physics 25

2.3.1 Geometry 25

2.3.2 Solving for Geodesic Equations 27

2.3.3 Apparent Solid Angle of the Hot Spot 28

2.3.4 Doppler Shift and Gravitational Redshift 29

2.3.5 Total energy flux contribution 31

2.3.6 The Oblate-shaped Neutron Star 31
2.4 Processing of Signals from NS to Detection 33
2.4.1 RX J0437.4-4711 34
2.4.2 Phase-dependent Power Law Component 35
2.4.3 ISM Attenuation 36
2.4.4 Effective Areas of *NICER* 37
2.4.5 Signal Management 38

3 Neutron Star Atmosphere Models 40
3.1 Format of the Intensity Profiles 41
3.2 Interpolation: Three Methods on Three Parameters 42
3.2.1 Temperature 42
3.2.2 Surface Gravity 48
3.2.3 Emission Angle to the Surface Normal 48
3.2.4 Two-point vs Four-point for Energy 49
3.2.5 Comparison of Intensity Profiles 50
3.3 Chapter Summary 53

4 Light Curve: Spectra and Waveforms 54
4.1 Parameters 55
4.1.1 Light Curve Settings 55
4.1.2 NS Configuration 57
4.1.3 Signal Processing 57
4.2 Effects of NS Parameters: A Toy Model 59
4.2.1 Spin 60
4.2.2 Temperature 62
4.2.3 Compactness 63
4.2.4 Radius 65
4.2.5 Second Spot 67
4.2.6 Colatitude and Inclination Angles 69

4.2.7 Atmosphere Models 70
4.2.8 ISM 71
4.2.9 Redistribution by *NICER*'s Response Matrix 72
4.3 Effects of NS Parameters: PSRJ0437 73
4.3.1 PSRJ0437 Statistics 73
4.3.2 Spectral Evolution with Phase 75
4.3.3 Waveform Evolution with Photon Energy 76
4.3.4 Comparison of Alternative Atmosphere Models 80
4.4 Chapter Summary 81

5 Conclusion **83**

List of Tables

3.1 Ranges and number of grid points for essential variables in NSX Hydrogen model 41

3.2 Ranges and number of grid points for essential variables in McPHAC hydrogen model 42

3.3 Power law interpolation error in intensity, for profiles of log(g) = 14.2 at various temperatures. 46

3.4 χ^2 values of each interpolation scheme for two- or four-point with respect to photon energy 50

4.1 Basic settings for the toy NS 59

4.2 Observation settings for the toy NS 60

4.3 Best PSRJ0437 parameters from previous efforts. Estimates not labelled are established by Bogdanov (2013). 74

4.4 Expected values in *NICER* observation on PSRJ0437 75

List of Figures

2.1 Rendering of specific intensity as differentials, adapted from Rybicki and Lightman (1979). 15

2.2 Surface gravity of NS given its mass and radius. 19

2.3 Two-point interpolation between data grid points, using linear or exponential schemes. Interpolated values for x = 6.5 are shown, illustrating the resulting errors. 20

2.4 If the energy band falls between two data grid points, we integrate with trapezoid rule. 22

2.5 If three data grid points are contained within the energy band, we integrate with trapezoid and Simpson's rules. 23

2.6 Spin-aligned coordinate system. Angles and axes in this diagram are defined in the text. 26

2.7 The final photon counts are consisted of various signal and background components. 34

2.8 ISM attenuation factors depends on hydrogen column density. . 37

2.9 *NICER*'s effective area changes with photon energy. 38

3.1 The intensity profiles are Planck-like and strongly dependent on temperature 43

3.2 The power law scheme consistently produces the lowest χ^2 per degrees of freedom of the three schemes. 44

3.3 Photon energy of maximum errors E_{max_e}, given a specific set of surface temperature and gravity. E_{max_e} increases with both temperature and gravity, and occurs at roughly the photon energy of peak intensity. 45

3.4 The upper panel shows the interpolations via the three schemes. The linear scheme is skewed by the profile of log(T) = 5.3, while the exponential scheme underestimates the intensities. The lower panel shows E_{max_e} of log(T) = 5.2 is near 0.1 keV for power law scheme. 47

3.5 Similar to Figure 3.4, the upper panel shows the interpolations via the three schemes and the lower panel shows E_{max_e} of log(T) = 5.2 for power law interpolation. E_{max_e} of log(T) = 5.2 is near 15 keV for power law scheme. 47

3.6 The intensity profiles is slightly flattened with increasing surface gravity. 48

3.7 Two-point and Four-point power law interpolation with respect to photon energy. Two-point interpolation consistently produces larger errors. 49

3.8 Comparison of Intensity Profiles at $T = 1.12 \times 10^6 K$. The difference between fully-ionized NSX Hydrogen and McPHAC Hydrogen models are barely noticeable. The partially-ionized NSX Hydrogen produces a softer profile, while NSX Helium produces a harder profile. 51

3.9 Comparison of Intensity Profiles at $T = 4.90 \times 10^5 K$ 52

3.10 Comparison of Intensity Profiles at $T = 2.00 \times 10^6 K$ 53

4.1 The waveform is distorted by the rapid rotation of the NS . . . 61

4.2 The spectrum is hardened by the Doppler boost 61

4.3 The spectra are Planck-like for their thermal nature. 62

4.4 The total numbers of photons follow the power law with respect to the temperature. 63
4.5 Higher compactness results in shorter eclipse 64
4.6 Higher compactness red-shifts the overall spectrum 64
4.7 Surface gravity values at constant compactness. The smaller the radius is, the larger the surface gravity gets. 65
4.8 Seeing the small change requires zooming into the rectangular area in the figure. 66
4.9 Influence of radius, thus surface gravity, on the observed spectrum. Decreasing the radius results in increases the surface gravity, which harden the high energy tail. 66
4.10 Waveform summed over all energies. Contribution by the second spot is located near phase = 0.5 67
4.11 Contribution by the second spot is clearly seen in the soft energy bands 68
4.12 Contribution by the second spot diminishes at harder energy bands 68
4.13 For $i = 50^o, \theta = 70^o$, no X-ray eclipse occurs even though the spot goes behind the Newtonian horizon momentarily. 69
4.14 Properties of the atmosphere intensity profiles are present on the resulting spectra 70
4.15 The general shape of the waveform remains the same with different atmosphere models. 71
4.16 The amount of ISM determines how many soft X-ray photons arrive at the detector. 72
4.17 The spectrum's peak photon count is shifted to higher energy by *NICER*'s response matrix 73
4.18 The contributions by the two hot spots are demonstrated with phase-specific spectra. The spectrum is harder when the hotter hot spot faces the observer. 76

4.19 Waveform at 0.12 keV. No contribution by the hot spots are present. 77
4.20 Waveform at 0.36 keV has the most counts of all energy bands. 77
4.21 Waveform at 0.53 keV has equal contributions from the two hot spots. 78
4.22 Waveform at 1.0 keV shows little contribution by the colder hot spot. 79
4.23 The total number of photons observed at 2.23 keV is only 5% of the number of photons at 0.36 keV. 79
4.24 The spectrum produced by McPHAC Hydrogen model agrees very well with NSX Hydrogen model 80
4.25 Compared to hydrogen, helium atmosphere produces less counts between 0.1 and 1.5 keV and slightly more counts above 1.5 keV. 81

List of Symbols

Symbol	Description
h	Planck's Constant
c	Speed of Light
e	Base Constant of Natural Logarithm
k_B	Boltzmann's Constant
g	Surface Gravity
G	Gravitational Constant
M	Mass of Neutron Star
R	Radius of Neutron Star
E	(Photon) Energy
I_ν	Specific Intensity
F_ν	Specific Flux
I	Total Intensity
F	Total Flux
p	Photon Number Flux
A	Cross-section of Interaction Effective Area of Detector
t	Time
Ω	Solid Angle
ν	Frequency
B_ν	Planck intensity function
T	Temperature
$\mathbf{r}$ & $\hat{r}$	Position/Direction Vector of Hot Spot
θ	Hot Spot Colatitude Angle
ϕ	Hot Spot Azimuthal Angle
i	Hot Spot Inclination Angle

ψ	Hot Spot Bending Angle
α	Emission Angle to Surface Normal
$\hat{k_0}$	Original Photon Direction
$\hat{k}$	Line of Sight Final Photon Direction
b	Impact Parameter
δ	Doppler Boost Factor
$\bar{\Omega}$	Rotation Parameter

Glossary of Terms

Abbreviation	Description
NS	Neutron Star
EOS	Equation of State
MSP	Millisecond Pulsar
LMXB	Low-mass X-ray Binary
UCXB	Ultra-compact X-ray Binary
PSRJ0437	Pulsar J0437-4715
McPHAC	McGill Planar Hydrogen Atmosphere Code
NICER	Neutron Star Interior Composition ExploreR

Chapter 1

Introduction

1.1 Neutron Star Basics

Since the discovery of neutron stars (NS) in the form of pulsars by Jocelyn Bell Burnell and Antony Hewish (Hewish et al., 1968), unsolved mysteries about NS still exist today. NS are the end products of massive star supernovae (Baade and Zwicky, 1934), and are formed by the immense gravitational pressure which compresses the core of the progenitor into a compact object. Matter is confined in some of the most extreme environments in the universe: mass of $\sim 1.4 M_{\odot}$ in ~ 10 km radius, magnetic field of up to 10^{15} Gauss (Olausen and Kaspi, 2014), rapid rotation at the timescales of milliseconds (Hessels et al., 2006), and high pressure and density in the interior.

NS are supported by various mechanisms, depending on the pressure-density regimes at different depths. The interior of the NS is supported by various degeneracy pressures, starting with electron, neutron, and exotic phases at its core (Cumming, 2016). The outer layer is supported by degenerate electrons similar to the case of white dwarfs. Deeper down towards the core, it becomes more favourable for electrons to combine with protons, causing neutron-rich material. Eventually, nuclei break up to form a sea of free neutrons and protons, with possible exotic phases at the core. The material is compressed to densities

larger than nuclear material at low temperature, which is difficult to test on Earth.

Describing matter requires an equation of state (EOS), which governs the interaction between particles in various conditions. The structure of the NS is governed by hydrostatic equilibrium, in particular the Tolman-Oppenheimer-Volkoff equation (Oppenheimer and Volkoff, 1939; Shapiro and Teukolsky, 1983) (also see (Stergioulas and Friedman, 1995) for methods of constructing neutron star structures). Solving for hydrostatic equilibrium using a candidate EOS provides a mass-radius relation for NS. With accurate measurement of the mass and radius of NS, we can put constraints on the candidate EOS (see a review by Watts et al. (2016) on the current progress). NS can be detected in a wide spectrum of electromagnetic radiation, providing various methods for measuring the NS mass and radius. New developments in X-ray instruments will allow for precise observations of faint objects, constraining unsolved problems of NS physics.

1.2 Neutron Star emission mechanism: radio, X-ray binaries, accretion, and rotation

NS were first discovered as radio pulsars. The radio emission originates from the misalignment of rotation and magnetic axes, with synchrotron radiation originating from electrons gyrating around magnetic field lines. Understanding of the NS spin evolution provides measurements of its magnetic field. The electron population is situated above the surface of the NS. If the emission light cylinder is positioned favourably, the NS can be observed as pulsars as the emission light cylinder is directed towards and away from the Earth periodically with the NS rotation (Lorimer and Kramer, 2005).

In the X-ray regime, NS are more often detected in a binary system. X-ray binary systems are classified by the mass of the companion to the compact ob-

ject. Low-mass X-ray binaries (LMXB) are systems with the companion being main-sequence star of type A or later, and in some cases a white dwarf if it is very evolved (White et al., 1995). The primary emission mechanism for NS in a LMXB is through the accretion of matter from a donor object. During periods of active accretion, matter falls onto the accretion disk, causing the system to be X-ray bright. The bright periods, lasting months to years, are known as outbursts. The accreting matter follows the magnetic field lines onto surface spots on NS, causing pressure and temperature build-up. Thermonuclear flashes occurs in the outer layer of the NS while the luminosity increases in magnitudes and peaks in X-ray. The thermonuclear flashes are called type I bursts (Lewin et al., 1995). Type I bursts, as well as accretion powered pulsations, happen in the timescale of seconds to hours.

While not in outburst, an accreting NS is in a low-luminosity period known as quiescence. The thermal radiation in this stage comes from cooling of the hot core dissipating into the crust (Brown et al., 1998). The emission is assumed to be from the entire surface and unpulsed. By modelling the thermal radiation originated from the entire surface of the NS, mass and radius can be measured simultaneously. Such analysis requires using a NS atmosphere model. We will discuss the development of NS atmosphere models in section 1.5. See Lattimer and Steiner (2014) for an example of mass-radius measurement for NS in quiescent LMXB, and Elshamouty et al. (2016) for an examination of the assumption that the whole surface emits.

For an X-ray pulsar that no longer experiences accretion, its emission is confined to small portions of the surface (Bogdanov et al., 2007). The portions of hot, X-ray emitting regions on the surface are known as hot spots. Return current reheats the hot spots, giving them long lifespan. Due to the low surface temperature of the hot spots, this type of NS is faint, so the ideal targets should be nearby and thermal radiation dominates its spectrum. This type of object is known as a rotation-powered pulsar. The spectrum is similar to NS

in quiescent LMXB. Incorporating NS atmosphere models governed by known radiative transfer equations and opacity data is essential for constraining the mass-radius relation of the NS.

1.3 Light Curve of the Neutron Star Hot Spots

A rotation-powered NS has properties that depends on time and photon energy. With ideal conditions, the timing properties can be extracted and be used jointly with the spectroscopic properties. The spectroscopic properties are known as the *spectrum* of an object, while the timing properties of the NS is known as the *waveform*. The periodic variations at short timescales originate from the rotation of the NS. Together, the two types of information are known as the *light curve* of the NS. Using all aspects of the light curve allow further constraints on the NS properties.

Similar to a radio pulsar, modulation in the detected X-ray waveform from a rotation-powered NS is a result of light-emitting region beaming towards our line of sight. Most of the pulsed X-ray emission originates from the surface hot spot. Other mechanisms such as accretion disk, inverse-Compton, and magnetospheric interaction could contribute to the pulsed and/or unpulsed X-ray emission. Thus, understanding the surface properties of the NS would require an ideal target that is mostly free of these additional mechanisms.

The theory of X-ray modulations caused by surface hot spots was presented by Pechenick et al. (1983). Later work by Miller and Lamb (1998) included the effects of the Doppler shift caused by rapid rotation. Poutanen and Gierliński (2003) established a systematic approach to model the light curve of SAX J1808.4-3658. Later work by Morsink et al. (2007), Cadeau et al. (2007), and Stevens et al. (2016) followed their general approach in the development of the light curve modelling codes, appropriate for rapid rotation (also see other recent works by Lo et al. (2013) and Miller and Lamb (2015)). A detailed description

in the construction of hot spot modelling can be found in section 2.3. First, solving for the geodesic equation gives the photon trajectory, specifically the bending of photon emission angle from the NS surface to the line of sight, which leads to the correct photon times of arrival at the detectors. Next, the observed extent of the hot spot on the NS is calculated by considering the impact parameter as a result of general relativity. Third, they accounted for the red/blueshifts of the photon energies caused by the Doppler boost from the rapid spin of the NS and gravitational redshift as a result of immense surface gravity. Finally, combining all of the described physical effects give a general formula for the calculation of flux contributed from the NS hot spots. Previous efforts showed that the oblate shape of rapidly rotating NS is a more important effect than the metric choice for the surrounding spacetime (Morsink et al., 2007; Cadeau et al., 2007). Accommodating the important general-relativistic effects would allow us to have a accurate model that can be used to find the properties of the NS.

1.4 Millisecond Pulsar and the Need for a Neutron Star Atmosphere Model

A millisecond pulsar (MSP) is thought to be the final stage for a NS found in a LMXB that experiences accretion throughout its lifetime. It is commonly accepted that MSPs are formed under the recycling scenario: a NS gains angular momentum from the accretion of matter from a donor object (Alpar et al., 1982). Evidence show that many MSPs formed through such mechanism are old, since they can be found in old globular clusters (Ransom et al., 2005). In the process of being spun-up, NS gain angular momentum and lose magnetic field strength (Shibazaki et al., 1989). In the meantime, a layer of light element material from the donor is accumulated on the surface of the NS. MSPs thus should have an atmosphere that is made of light elements in a low mag-

netic field environment. The atmosphere is most likely made of hydrogen if the donor is a main sequence star, but could potentially be made of helium or heavier elements if the progenitor of the system is an ultra-compact X-ray binary (UCXB) (Nelemans et al., 2006) with a hydrogen-poor donor. Other than X-ray, millisecond pulsars are also a source of gamma-ray (see Johnson et al. (2014) for observations of millisecond pulsars in gamma ray).To accurately obtain measures of the MSP mass and radius using light curve modelling method, NS atmosphere models that can describe the surface emission are thus needed.

1.5 Brief Overview on the Neutron Star Atmospheric Models

Soft X-ray emission from a NS has a thermal origin. Modelling a NS atmosphere requires the use of standard radiative transfer equations along with several fundamental assumptions. Since rotation-powered NS are powered by the steady-state radiation as a result of NS cooling, hydrostatic and thermal equilibrium of a static atmosphere are generally assumed. The thin atmosphere of the NS ($\sim$1cm) (Romani, 1987) also means that the plane-parallel approximation can be used. Our project models light curves from MSPs, thus we should consider atmospheric models with low magnetic field. With these assumptions set, modelling the intensity profile from a NS atmosphere would require solving for temperature and pressure gradient iteratively along with some opacity database or an alternative method to obtain the opacity. The atmospheric models are improved over time by either refining assumptions to be closer to the physical reality, increasing accuracy and precision for the calculations, or incorporating effects that were not considered before. The next paragraphs will briefly talk about the early atmospheric models and improvements made by the modern approaches.

Romani (1987) made the first attempt to construct a cooling NS atmosphere model with several compositions of interest, and present-day models typically follow the same approach. The motivation was the observation by the *Einstein* X-ray telescope in the early 1980s, which allowed for the direct detection of thermal X-ray radiation from the surface of a NS. However, a simple blackbody fit often deviated from the observed spectrum, as a radiative atmosphere on the surface of NS would modify the inherent thermal radiation. A model that considered the radiative transfer properties of the NS atmosphere was thus needed. The general approach of Romani was to construct a starting approximation of temperature and pressure gradient using a gray atmosphere, and then to iteratively correct for the gradients by using radiative transfer equations and opacities for specific materials considered. A gray atmosphere is built on the assumption that the opacities are independent of photon energies (Carroll and Ostlie, 2007). In particular, Romani chose to build the temperature gradient using Rosseland mean opacity, which is defined as a grand average scheme of absorption and scattering coefficients scaled by the Planck function[1] (Rybicki and Lightman, 1979). One additional thing to note is that Romani obtained the material opacities through the Los Alamos Astrophysical Opacity Library data release of 1977 (Huebner et al., 1977); the opacity data is required to apply the radiative transfer equations. Other than using the three atmospheric compositions of interest, the paper also suggested the use of pure light element atmosphere in the future, as calculations showed that the immense gravity of a NS would force the heavier elements to sink away from the light element layer. The Romani model set the standard approach for modelling NS atmospheres, and provided several important implications that stood the test of modern efforts.

In 1995, Rajagopal and Romani (1996) (hereby R&R) revisited the previous effort made by Romani eight years earlier by putting further care in the

[1]See equation 1.110 of Rybicki and Lightman (1979)

use of opacity data. This was motivated by the new data release from the OPAL project with opacity data (Iglesias et al., 1987), as well as new instruments such as *ROSAT* which had the capability of identifying MSPs with low magnetic field. The OPAL project provided additional insight by using full spin-orbit coupling states of iron, and calculated the full atmospheric EOS tables, which gave pressure gradient as a function of temperature and density. This allowed for a more accurate pressure gradient model as compared with the previous effort, which used an estimate and iteratively corrected using just the hydrostatic equilibrium condition. They also calculated a hydrogen atmosphere model, which was suggested in the previous efforts of Romani, since a pure light element atmosphere is most likely due to the immense gravity of NS. The models R&R calculated include blackbody, three atmosphere compositions of pure hydrogen, solar mixture, and iron, and two models with strong magnetic field. R&R applied several models to the ROSAT observation of the nearby isolated X-ray pulsar J0437-4715 (hereafter PSRJ0437). First discovered by Johnston et al. (1993), PSRJ0437 is the closest isolated MSP, with a distance of 156.3 parsecs (measured by Deller et al. (2008)). R&R found that the non-magnetized pure hydrogen atmosphere was the most likely explanation for J0437. The 5.5 day orbital period (Johnston et al., 1993) with its companion means it is not an UCXB, which makes it unlikely to have non-hydrogen atmosphere. In addition, the best fit parameters are consistent with the picture of a NS with polar hot spots. This marked the first application of the NS atmosphere model to a rotation-powered X-ray MSP.

At around the same period of time, Zavlin et al. (1996) (hereby ZPS) developed an alternative atmosphere modelling method which has focuses on both composition and anisotropy. In additional to the new data release of OPAL, the need for low magnetic field models, and the need to consider a hydrogen atmosphere, they also investigated the effect of anisotropy of the surface emission. The anisotropy is caused by the fact that photons emitted parallel to

the surface come to the surface from shallower layers of the atmosphere, while photons emitted normal to the surface come from deeper layers of the atmosphere. Investigation of the anisotropy was needed to account for the effect of limb-darkening on the NS hot spots, as well as anisotropy in the heat conduction of NS crust, which inherently affects the emergent intensity profile. By starting with boundary problems extending from the existing radiative transfer equation, they provided an alternative approach from R&R and thus had an independent model for comparison. Applying their models to the observation of PSRJ0437, hydrogen models again seemed to be the most physically likely. Compared with the results of R&R, there were differences in the best-fit parameters such as higher temperature and smaller surface hot area, albeit the difference could be a result of consideration of anisotropy and gravitational lensing.

NSATMOS is one of the most utilized modern NS atmosphere model for its completeness and availability. Its assumptions are widely-accepted and it is available in XSPEC for application to observations. This model was first developed by McClintock et al. (2004) and Heinke et al. (2006), while Heinke et al. (2006) applied the model to the observation of a NS in 47 Tucanae by *Chandra*. Continued from previous efforts, assumptions such as plane-parallel static atmosphere, negligible magnetic fields, hydrostatic equilibrium were still applied, with additionally specified conditions that clarify the validity of the model. Omission of Comptonization somewhat over-estimated the hard tail of the intensity profiles at high temperature, and assumption of full ionization would discard contribution of opacity from absorption lines of neutral hydrogen. On the other hand, full ionization meant opacity can be solved analytically by simply finding the ideal EOS and components of free-free and Thomson scattering between protons and electrons, instead of the usual OPAL library data. Additional improvements included accounting for self-irradiation, rewriting variables in transfer equations in terms of Eddington factors to improve accuracy,

and new ways of correcting for temperature structure. Improved techniques in solving for the atmosphere structure made this model more reliable and better resembled the physical reality of the NS hydrogen atmosphere.

The McGill Planar Hydrogen Atmosphere Code (McPHAC) was created by Haakonsen et al. (2012) aiming to achieve low computational uncertainty in modelling hydrogen atmosphere on a low magnetic field NS. Constraining the NS parameters via the full light curve method to low uncertainty requires intensity profile models to have a even lower uncertainty. With the development of an open-source code that had the capability of limiting computational error, high accuracy could be achieved while keeping the flexibility for users to reflect different assumptions of the model. The default assumptions were similar to NSATMOS, but a few phenomena were not modelled since they were not deemed important through previous studies: electron conduction was omitted, self-irradiation was ignored, and radiation pressure was neglected. The general set up and solution of the model was similar to ZPS, but several improvements were made. First, to account for the opacity to the fullest extent, McPHAC combined both the Opacity Project opacity data and free-free opacity for ionized hydrogen together, accounting for the varying degree of ionization as determined by OPAL library's EOS at different temperature. Neutral hydrogen could dominate opacities at certain frequencies near the spectral lines. Next, investigation of anisotropic Thomson scattering showed a small hardening of the intensity profiles, although isotropic scattering could be assumed if the limit in uncertainty is no greater than 1%. Choosing isotropic scattering would also allow the use of Rybicki-type solution (Rybicki, 1971), which would speed up the temperature correction scheme of the model. The Rybicki-type solution rewrites the matrix problem related to the temperature corrections into tridiagnoal matrices, which are less computationally demanding to invert (Haakonsen et al., 2012). Finally, investigation in computational error could be split into error caused by truncation or caused by convergence. Truncation

error occurred with the discretization of the variables, which was necessary for the numerical method. The errors could be limited to less than 0.01% if enough steps are taken in depth and angle variables for solving the radiative transfer equation. Correction in temperature profile was limited to less than 0.01% after five iterations, which showed good convergence of the model. With extensive efforts in reflecting known physics and limiting error, McPHAC is a state of art in modelling hydrogen NS atmosphere.

NS could have surface composition made of material heavier than hydrogen if the accretion donor is hydrogen-poor (i.e. a carbon-oxygen white dwarf). UCXB is the progenitor for this type of system. NSX is a series of atmosphere models with various surface compositions, including pure light elements such as hydrogen, helium, carbon, nitrogen, or oxygen (Ho and Heinke, 2009). The models were originally developed for application to quiescent low-mass X-ray binary, although they were applied to X-ray observations of the central compact object of Cassiopeia A first. Cassiopeia A was one of the youngest supernovae remnants. The construction of such models followed consistent assumptions of a plane-parallel atmosphere in hydrostatic and radiative equilibrium. The opacity data was obtained from the Opacity Project. The light element atmosphere models produced intensity profiles that were harder than blackbody, which was due to energy-dependence of the opacities, and this phenomenon was already predicted by the previous work of R&R and ZPS. A newer version of NSX atmosphere models with compositions of hydrogen and helium have been computed by Ho (2017). With the consideration of other light element atmosphere models, we can obtain alternative fittings to observation that may be better representing the physical realities of the NS.

1.6 Next Generation Instruments: *Astrosat* and *NICER*

With their exceptional capability in timing and large collecting area, *Astrosat* and Neutron Star Interior Composition ExploreR (*NICER*) will become essential for the observation of NS thermal emission. *Astrosat* is a new multi-wavelength observatory with the capability to simultaneously observe an object from near-UV to hard X-ray (Singh et al., 2014). It is India's first space telescope, and Canadians have made significant contribution to the project. *Astrosat*'s Large Area Xenon Proportional Counter (LAXPC) has an effective area of 8000 cm^2 at for photons between 5 to 20 keV, and it will produce high photon counts for observation of accretion-powered X-ray pulsar such as SAX J1808.4-3658. *NICER* is an newly-launched NASA telescope optimized to conduct X-ray pulsar observations (Arzoumanian et al., 2014). Launched in June 2017, its excellent timing and spectroscopic resolution is best suited to observe rotation-powered X-ray MSPs, with PSRJ0437 as its primary target. The stable emission from the surface hot spots of PSRJ0437 will provide an excellent application for this thesis project. Other proposed projects, such as the former *LOFT* (Feroci et al., 2012) and the future *eXTP* (Zhang et al., 2016) and *Strobe-X* (Wilson-Hodge et al., 2017), are also designed with similar concepts. The new telescopes will allow the astronomers to further constrain the properties of the NS.

1.7 Organization of the Thesis

Chapter 2 introduces the physical and mathematical concepts used in this thesis work. The concepts can roughly be split into four themes: radiation basics, interpolation and integration, NS hot spot mechanics, and process of the signals from NS to detector photon counts. Chapter 3 explores the intensity profiles

produced by modern NS atmosphere models. The analysis includes interpolation properties and differences between different surface compositions. Chapter 4 describes the light curves produced by NS hot spot modelling with applications of different atmosphere models and instrumental effects. We discuss the effects of parameters on the spectra and waveforms via simulations of a toy model for *NICER*'s observation of PSRJ0437.

Chapter 2

Mathematical Background

The main focus on my thesis project is to bridge the gap between existing NS light curve models with observational data. This section consists of the tools used to accomplish this goal. The first section derives several measures of radiation, including specific intensity, energy flux, and photon counts. The second section contains numerical formulas, including interpolation and integration, which allow us to manipulate the existing atmosphere models into measurable quantities of the NS. The third part of this chapter describes the convention for NS hot spot, as well as physical phenomena that need to be accounted for in modelling the light curve. The last part of this chapter describes the processing of signals, independent of the influence of the NS, into photon counts as observed by the telescopes, with main focus on the adaptation for future *NICER* observation.

2.1 Radiation Basics

The most fundamental measure of radiation starts with the *Specific Intensity*, which measures the energy carried by an infinitesimal light ray. Specific intensity describes the properties of the source, which in turn are interpreted by the astronomers to understand the physical phenomenon happening at the source.

We will work our way up to construct measurable quantities by the telescopes from the specific intensity.

Specific intensity is usually denoted by the symbol I_ν, with the subscript ν symbolizes that it is the intensity at a specific frequency or photon energy. We define the term *intensity profile* being the set of specific intensities as a function of energy given a particular set of NS conditions. Specific intensity is (Rybicki and Lightman, 1979)

$$dE = I_\nu \; dA \; dt \; d\Omega \; d\nu, \tag{2.1}$$

where the source's specific intensity is related to the total energy dE, from the source crossing an area dA, in the time interval dt, directed at an angle α from the surface normal within the solid angle $d\Omega$, and within the frequency bandwidth of $d\nu$. There are good discussion of specific intensity in most standard textbooks on radiation processes. An adaptation from Rybicki and Lightman (1979) is shown in Figure 2.1

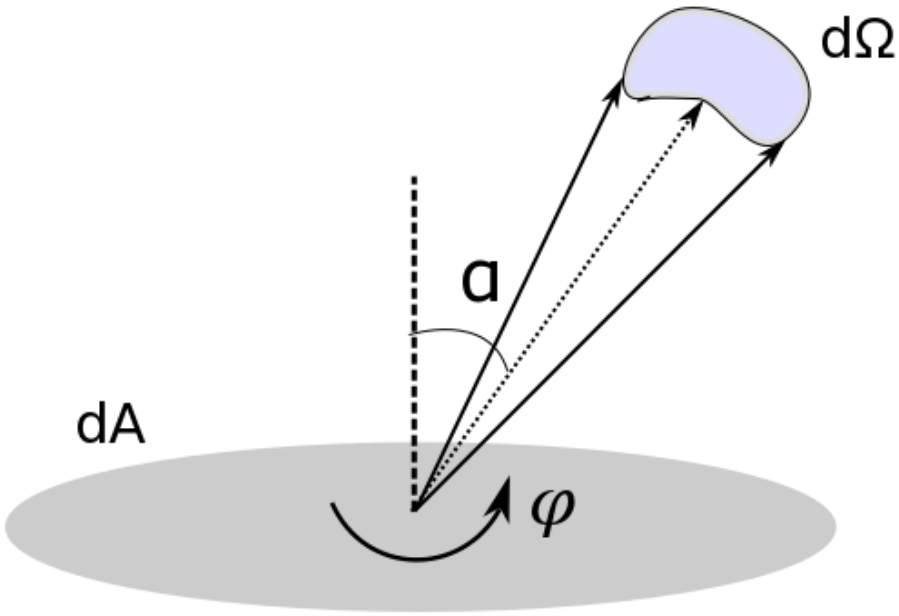

Figure 2.1: Rendering of specific intensity as differentials, adapted from Rybicki and Lightman (1979).

For a source in local thermal equilibrium, it emits blackbody radiation, which is well described by Planck's function

$$B_\nu = \frac{2h\nu^3}{c^2} \frac{1}{e^{\frac{h\nu}{k_B T}} - 1}, \tag{2.2}$$

where B_ν is the specific intensity of a blackbody, h is Planck constant, c is the speed of light, k_B is Boltzmann constant, and T is the temperature of the source. The specific intensity of blackbody radiation depends only on the temperature of the object and the frequency. Note that blackbody radiation is *isotropic*, which means that the radiation strength is independent of the angle from the surface normal, α, that it is emitted from.

The energy flux received by a detector needs to account for all contributions of the source specific intensities across some bandwidth and the solid angle in which the object subtends. The energy flux F_ν is defined by (Rybicki and Lightman, 1979)

$$F_\nu = \int I_\nu cos(\alpha) d\Omega. \tag{2.3}$$

The $cos(\alpha)$ term gives the projection of the emission surface onto the imaginary surface perpendicular to the direction towards the observer. For a spherical object, we can further break the solid angle integral into polar and azimuthal components

$$F_\nu = \int_0^{2\pi} d\varphi \int_0^{\pi/2} I_\nu(\alpha) cos(\alpha) sin(\alpha) d\alpha. \tag{2.4}$$

Note that when observing an isotropic source with no α dependence, such as blackbody, from very far away, the integral would simplify to πI_ν. However, this will not be true if the source object is either not spherical, not isotropic, or is only partially illuminated over its spherical surface. In practice, we find the angular and frequency dependence piece-wise, and sum all of the contributions to obtain the flux of the entire source.

Further integrating F_ν over the bandwidth of the detector would give the energy flux F. However, X-ray detectors keep track of their observations through photon counts. To convert a modelled energy flux into predicted photon count rates of a detector, the specific intensity should be divided by its photon energy to be converted into photon intensity. Consider the following integral

$$I = \int_{\nu_o}^{\nu_f} I_\nu d\nu, \tag{2.5}$$

where the total intensity is obtained by integrating the specific intensity over a bandwidth from ν_o to ν_f. If we do a change of variable and define $y = log(\nu)$, then

$$dy = \frac{1}{\nu} d\nu, \tag{2.6}$$

$$d\nu = \nu dy, \tag{2.7}$$

$$I = \int_{y_o}^{y_f} I(y)\nu dy. \tag{2.8}$$

The photon number flux p is defined by

$$p = \int_{y_o}^{y_f} I(y)\frac{\nu}{(h\nu)} dy = \int_{y_o}^{y_f} \frac{I(y)}{h} dy. \tag{2.9}$$

The variable change gives two advantages: first eliminating the need to divide the integrand intensity by its energy, and the second making use of the log-spaced energy grid that most NS atmosphere intensity profiles are available in. The two advantages allow for easy implementation of numerical integration to find the correct photon flux.

2.2 Numerical Formulas for Interpolation and Integration

Obtaining measurable quantities from light curve simulation from intensity profiles requires integration, as explained by the previous section. However, the integral of Planck's function cannot be obtained in an indefinite form, and the intensity profiles for realistic atmosphere models are certainly not blackbody and not analytical. However, since the emission is thermal in nature, the intensity profiles for light-element atmosphere models are essentially continuous, with a few absorption edges from partial ionization if included in the model. We can apply numerical methods to interpolate the intensity profiles of NS atmosphere models from its given energy, emission angle to normal, surface gravity, and temperature grid to obtain specified values needed, as well as methods to integrate the interpolated values to measurable quantities for light curve modelling.

2.2.1 Interpolation

The NS atmosphere intensity profiles are available with a given set of values for the temperature and surface gravity. The surface gravity, g, for a spherical, non-rotating NS can be calculated with the relativistic gravity formula

$$g = \frac{GM}{R^2} \frac{1}{\sqrt{1 - \frac{2GM}{Rc^2}}}, \tag{2.10}$$

where G is the gravitational constant, M is the mass of the NS, and R is the radius of the NS. Typical range of surface gravity of NS is shown in Figure 2.2.

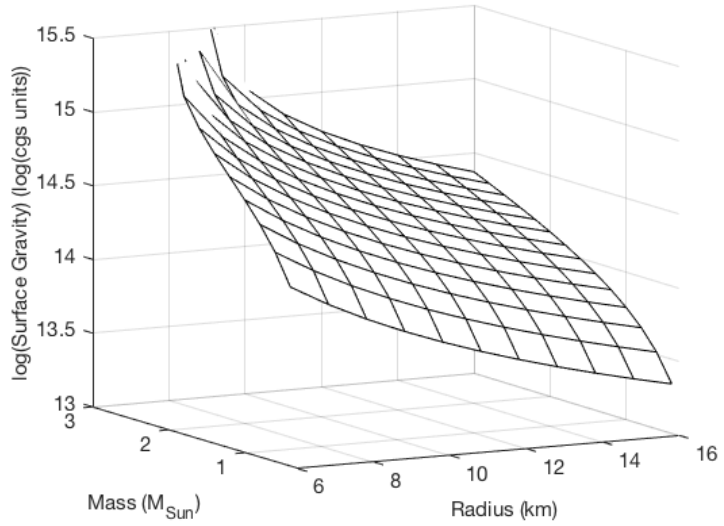

Figure 2.2: Surface gravity of NS given its mass and radius.

The surface gravity for oblate, rapidly-rotating NS is described in section 2.3.6. If we want to find the intensity profile for a choice of temperature and surface gravity that is not available directly from the given set, we must interpolate from the available intensity profiles. Since there are four parameters that need to be considered: photon energy, emission angle to normal, surface gravity, and temperature, it would be computationally costly to interpolate over more than just the two closest values. Due to the thermal nature of the intensity profiles, the intensity values vary quickly with temperature. We can interpolate the intensity profiles in three possible schemes: linear interpolation, which means fitting a straight line with one of four parameters as our independent variable and intensity as dependent variable; semilog interpolation, which means fitting a straight line with the parameter as the independent variable but take the logarithmic value of intensity as dependent variable; and log-log interpolation, which means fitting a straight line to the logarithmic values of both the parameter and intensity. Each of the three interpolation method represent an underlying scheme. Interpolating linearly represent the theoretical scheme

$$I = aT + b, \tag{2.11}$$

while taking the logarithmic of the intensity represent the exponential law

$$I = e^b e^{aT}, \tag{2.12}$$

and taking the logarithmic of both the temperature and intensity represent the power law

$$I = e^b T^a. \tag{2.13}$$

The intensity values follow approximately the power law when interpolating through temperature, because the Stefan-Boltzmann Law $F = \sigma T^4$ is in the power law form. If we were to use an inappropriate fitting scheme, the result could create large error.

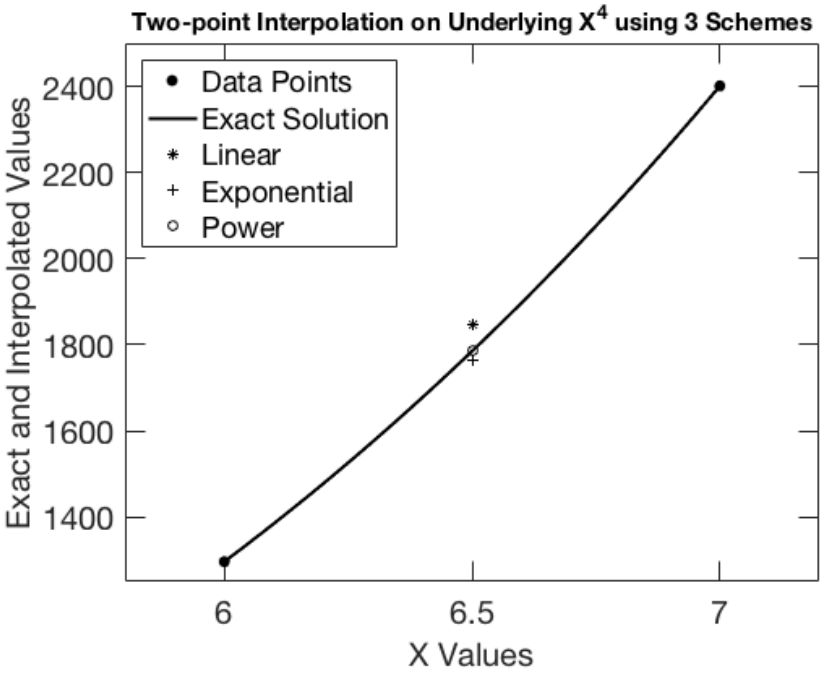

Figure 2.3: Two-point interpolation between data grid points, using linear or exponential schemes. Interpolated values for x = 6.5 are shown, illustrating the resulting errors.

Figure 2.3 is a demonstration using two-point interpolation of an underlying power law using the three schemes. The linear scheme produces the largest deviation from the exact solution, while the power law scheme interpolates to the exact solution.

Suppose that we want to find the intensity at temperature T for photon energy E, with all other variables held constant, and the closest temperature grid values are T_1 and T_2. The interpolated value of intensity can be calculated with the two-point interpolation formula

$$I(T,E) = exp\Bigg\{ log(I(T_1,E)) + \Big[log(I(T_2,E)) - log(I(T_1,E)) \Big] \Big[\frac{log(T) - log(T_1)}{log(T_2) - log(T_1)} \Big] \Bigg\}. \tag{2.14}$$

In practice, we interpolate between 32 intensity values: 2 for each of the temperature, surface gravity, and angle to surface normal, and 4 for the photon energy. We interpolate logarithmically in the order of energy, emission angle to normal, surface gravity, and finally temperature. This is to ensure that interpolation error is minimized, since the intensity values is sensitive mostly to temperature. We justify the chosen interpolation method in section 3.2.

2.2.2 Integration

Once we are able to find the intensity profile for a specific set of parameters, we have to integrate over the energy bandwidth to find total intensity. If all of the intensity profiles are available with the same energy grids, it is possible to skip interpolation in energy and instead use the energy grid to conduct discrete integration for some part of the total flux. Note that interpolation over other variables still needs to be done, and almost always will we end up with bandwidth edges that requires integration over all variables. We will discuss how to integrate over the energy bandwidth, with dependence on the bandwidth limits and the size of the bandwidth. All of the discrete integration

routines used in this work can be found in *Numerical Recipes* by Press et al. (2007).

The trapezoid rule is the simplest of all. The formula is the same as calculating the area under the curve that has the shape of a trapezoid. The trapezoid is made of four sides, with three sides being the lines from the data points to the x-axis and the x-axis under the curve, while the last side is the straight line between the two data points. The formula is

$$\int_{x_0}^{x_1} f(x)dx = h\left[\frac{1}{2}f_0 + \frac{1}{2}f_1\right] + O(h^3 f''), \tag{2.15}$$

where h is the difference between x_0 and x_1, and O is the error term. The error term arises from approximating the real curve with a straight line between the two data points. This convention will be used for the other formulas in this section. Figure 2.4 is a demonstration of the trapezoid rule.

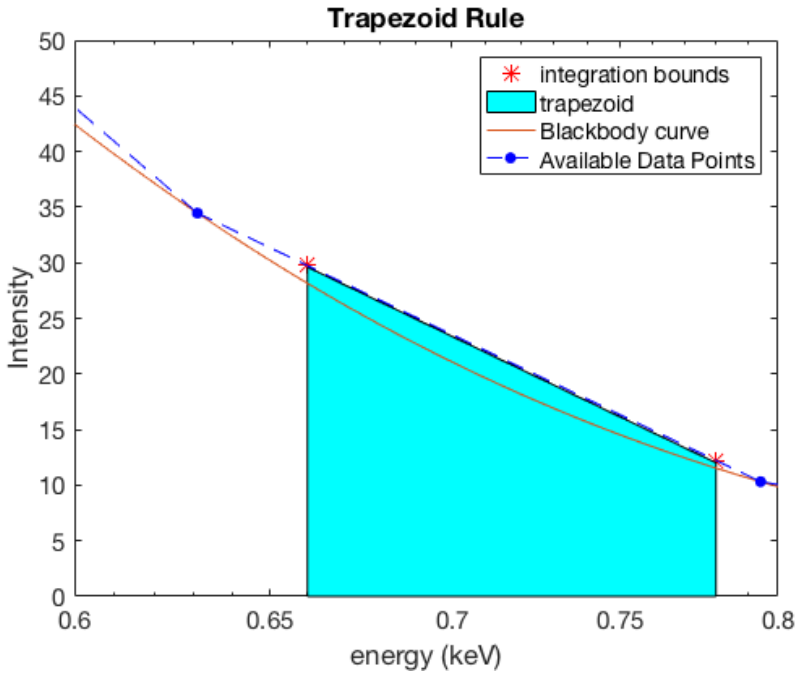

Figure 2.4: If the energy band falls between two data grid points, we integrate with trapezoid rule.

The trapezoid rule is very important, since the bandwidth boundaries never

falls exactly on the energy grid, and integration always requires using trapezoid rule to integrate to the closest energy grid point. This is the most used rules of all integration routines described in this work. When there are more than three energy grid points available within the bandwidth, other than using trapezoids at the edges of the bandwidth, integrating between the available energy grid points requires the use of Simpson's rule

$$\int_{x_0}^{x_2} f(x)dx = h\left[\frac{1}{3}f_0 + \frac{4}{3}f_1 + \frac{1}{3}f_2\right] + O(h^5 f^{(4)}). \tag{2.16}$$

x_0, x_1, and x_2 are the three energy grid points; f_0, f_1, and f_2 corresponds to the values of the function at x_0, x_1, and x_2, respectively; h is the difference between two energy grid points. Figure 2.5 is a demonstration of Simpson's rule used in combination with trapezoid rule.

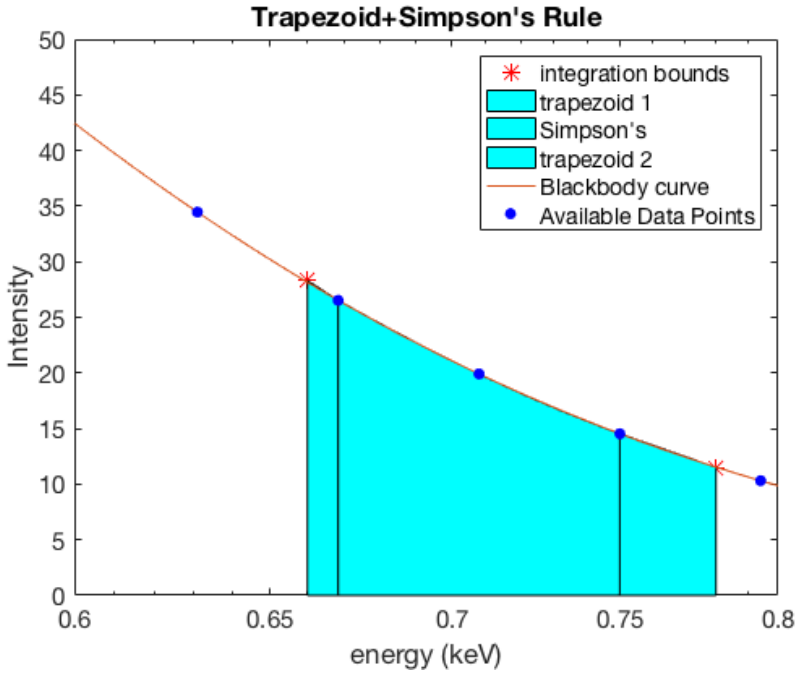

Figure 2.5: If three data grid points are contained within the energy band, we integrate with trapezoid and Simpson's rules.

Note that the coefficients add up to 2, which makes sense since the integration is done across the width of $2h$. When there are four data points available,

we use Simpson's $\frac{3}{8}$ rule

$$\int_{x_0}^{x_3} f(x)dx = h\Big[\frac{3}{8}f_0 + \frac{9}{8}f_1 + \frac{9}{8}f_2 + \frac{3}{8}f_3\Big] + O(h^5 f^{(4)}). \tag{2.17}$$

For five data points available, we use *extended Simpson's rule*

$$\int_{x_0}^{x_4} f(x)dx = h\Big[\frac{1}{3}f_0 + \frac{4}{3}f_1 + \frac{2}{3}f_2 + \frac{4}{3}f_3 + \frac{1}{3}f_4\Big] + O(\frac{1}{N^4}). \tag{2.18}$$

For six or more data points, we use a formula that has the same order as the extended Simpson's rule

$$\int_{x_0}^{x_{N-1}} f(x)dx = h\Big[\frac{3}{8}f_0+\frac{7}{6}f_1+\frac{23}{24}f_2+f_3+f_4+...+\frac{23}{24}f_{N-3}+\frac{7}{6}f_{N-2}+\frac{3}{8}f_{N-1}\Big]+O(\frac{1}{N^4}). \tag{2.19}$$

The rule is obtained by using cubic polynomial solutions for each successive groups of four points. All of these rules are implemented in this work and are used in simulations when needed. In general, when producing model light curves for *NICER*, rules beyond Simpson's rule are rarely used, since the bandwidth for *NICER* is small compared with the energy grid we are provided with.

2.3 NS Hot Spot Physics

Radiation coming from a hot spot of finite size on a NS is subject to special and general relativistic effects. In order to model such effects, we first introduce the conventions for a NS and its hot spots. Once the conventions are established, we can calculate a series of parameters associated with the relativity effects. There are several effects that affect the contribution of photon counts by the hot spot. Due to the immense spacetime distortion caused by the NS, we solve the photon geodesic equations in Schwarzschild metric. The solutions can be used to calculate photon tracks and thus the original angle of emission as well as time of arrival of the photons. The relativistic rotation of the NS causes a Doppler boost, which affects the apparent size and temperature of the hot spot. Finally, the redshift of the photon caused by the distorted spacetime is calculated. This approach, known as the Schwarzschild plus Doppler approximation, was described in detail by Poutanen and Gierliński (2003). We follow this general approach with corrections from the oblate-shaped geometry of a NS in order to have a complete picture of the radiation from the hot spots.

2.3.1 Geometry

Two coordinate systems are used to derive the relativity effects in this work: spin-aligned and velocity-aligned. The most intuitive formulation is to set the origin at the centre of the NS and define the x-axis $\hat{x}$ as the spin-axis. This is called the spin-aligned system. The position of an infinitesimal spot on the NS surface $\mathbf{r}$ defined in spherical coordinates as

$$\mathbf{r} = R\hat{r} = R(cos(\theta)\hat{x} + sin(\theta)sin(\phi)\hat{y} + sin(\theta)cos(\phi)\hat{z}), \tag{2.20}$$

where the angles θ and ϕ are defined in Figure 2.6.

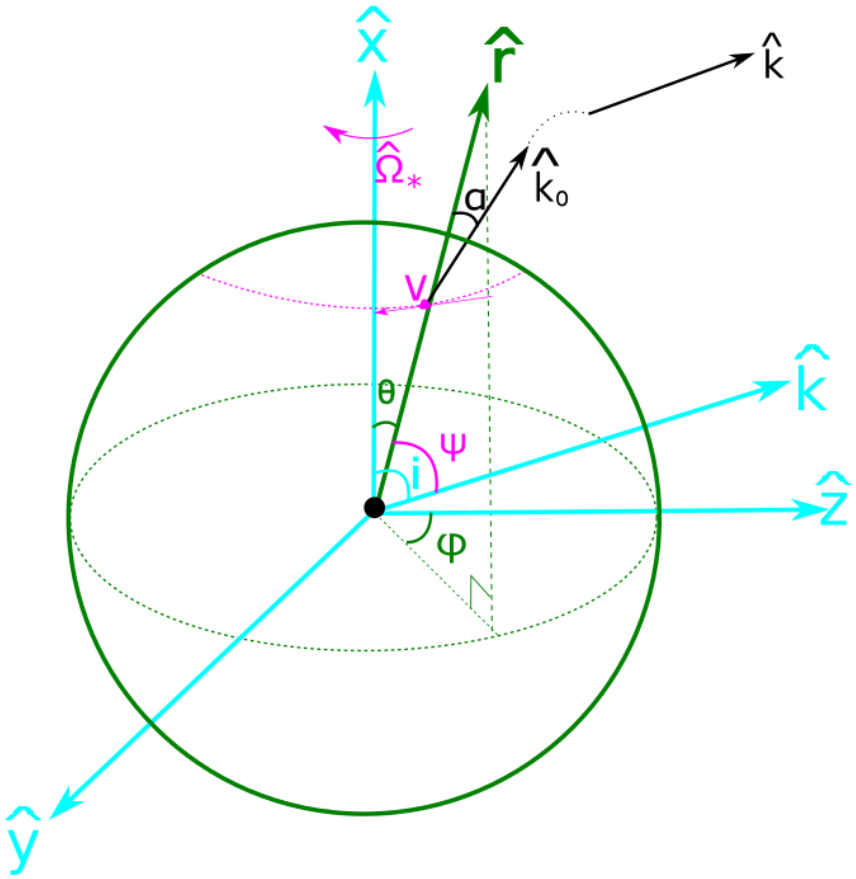

Figure 2.6: Spin-aligned coordinate system. Angles and axes in this diagram are defined in the text.

We define the colatitude angle θ as the angle between $\hat{r}$ and $\hat{x}$. Therefore, it is natural to define the azimuthal angle ϕ as the angle between $\hat{z}$ and projection of $\hat{r}$ on the y-z plane. The direction to the observer is $\hat{k}$, and is not particularly aligned with any of the three Cartesian axes.

For a hot spot with finite size, we split the hot spot into pieces, approximate each piece as having the same position vector over the entire piece, and calculate the full light curve from the hot spot by summing the contributions of the several pieces.

2.3.2 Solving for Geodesic Equations

Due to the immense spacetime curvature around the NS, the photon's direction changes from the initial direction $\hat{k_0}$ to the directions towards the observer $\hat{k}$. The photon is originally emitted at angle α to the surface normal, which for the case of spherical star is $\hat{r}$

$$cos(\alpha) = \hat{k_0} \cdot \hat{r}. \tag{2.21}$$

The direction towards the observer, k, is in the x-z plane and defined with the inclination angle i

$$\hat{k} = cos(i)\hat{x} + sin(i)\hat{z}. \tag{2.22}$$

The bending angle, ψ, is the angle between the direction to the spot and the direction towards to observer. $cos(\psi)$ is defined as the angle between $\hat{k}$ and $\hat{r}$

$$cos(\psi) = \hat{k} \cdot \hat{r} = cos(i)cos(\theta) + sin(i)sin(\theta)cos(\phi). \tag{2.23}$$

The Newtonian horizon limits the photons to be visible with bending angles $|\psi| < \pi/2$, while General Relativity allows a photon to be visible for $|\psi| > \pi/2$ should enough bending due to gravity occurs.

Due to the spherical symmetry of the Schwarzschild metric, the trajectory of the photon is confined to a plane so that the final photon direction is a linear combination of the initial photon direction and position vectors

$$\hat{k} = \frac{1}{sin(\alpha)}(sin(\psi)\hat{k_0} + sin(\alpha - \psi)\hat{r}). \tag{2.24}$$

We require α to obtain the correct specific intensity of the emission, since the NS atmosphere model emits anisotropically. The impact parameter, b, is defined as (Pechenick et al., 1983)

$$b = \frac{R}{\sqrt{1 - r_g/R}} sin(\alpha), \tag{2.25}$$

where the Schwarzschild radius is denoted by $r_g = 2GM/c^2$, where M is mass of the NS. The solution of ψ is dependent on b (Pechenick et al., 1983),

$$\psi(b) = \int_R^\infty dr \frac{b}{r} \Big[1 - \frac{b^2}{r^2}(1 - \frac{r_g}{r})\Big]^{-1/2}. \tag{2.26}$$

Even though there could be singularities in the integral, the singularities are integrable and indefinite integrals can be found. In practice, we specify M, R, θ, ϕ, and i. First, we use Equation 2.23 to compute the required bending angle ψ. Then, Equation 2.26 is inverted to solve for the value of b which allows a photon to travel from location (θ, ϕ) to an observer at angle i. Finally, the angle α can be found given Equation 2.25. Even though previous efforts in hot spot modelling often choose to use a less computation-heavy approximation (Bogdanov et al., 2007), we opt to use the full integral and produce a look-up table for the bending angles.

2.3.3 Apparent Solid Angle of the Hot Spot

In a flat spacetime geometry, $d\Omega$, the solid angle of a source, is related to $dA_\perp$, the projection of the emission area perpendicular to the line of sight, and D, the distance to the NS (Carroll and Ostlie, 2007)

$$d\Omega = \frac{dA_\perp}{D^2} = \frac{dScos(\alpha)}{D^2}. \tag{2.27}$$

In Newtonian gravity, the emission surface is defined by $dS = R^2 sin(\alpha) d\alpha d\varphi$. We can write $dA_\perp$ in the impact factor format (Poutanen and Gierliński, 2003)

$$dA_\perp = bdbd\varphi. \tag{2.28}$$

Making use of the relation between b, ψ, and α, the solid angle is (Poutanen

and Gierliński, 2003)

$$d\Omega = \frac{dA_{\perp}}{D^2} = \frac{R^2}{D^2}\frac{1}{1 - r_g/R} sin(\alpha) cos(\alpha) d\alpha d\varphi. \tag{2.29}$$

We change the variable to the bending angle ψ to give (Poutanen and Gierliński, 2003)

$$d\Omega = \frac{R^2}{D^2}\frac{1}{1 - r_g/R} cos(\alpha)\frac{dcos(\alpha)}{dcos(\psi)} dcos(\psi) d\varphi. \tag{2.30}$$

To speed up the computation, we pre-compute the derivatives associated with the bending angle to produce a lookup table to be used in the computation.

2.3.4 Doppler Shift and Gravitational Redshift

Relativity modifies the intensity profile via two effects: Doppler shift from special relativity and gravitational redshift from general relativity. In this section, we will describe how the two effects modify both the intensity values and the photon energies of the intensity profile. We follow the derivation of Poutanen and Gierliński (2003). The speed of the spot v is

$$v = \frac{R\Omega_*}{c}\frac{1}{\sqrt{1 - r_g/R}} sin(\theta), \tag{2.31}$$

where Ω_* is the rotation of the NS defined in Figure 2.6. Doppler shift for the signal can be found by the formula

$$\delta = 1/(\gamma(1 - \beta cos(\xi))), \tag{2.32}$$

where $\beta = v/c$, and $\gamma = (1 - \beta^2)^{-1/2}$ are the standard relativity-related quantities. ξ is the angle between the velocity of the spot and k_0, so the $cos(\xi)$ factor shows the direction component of the emission that is parallel to the velocity of the hot spot. Finding the Doppler shift factor is most easily done in the velocity-aligned coordinates. The direction of the hot spot velocity $\hat{v}$

depends on ϕ

$$\hat{v} = \hat{r} \times \hat{x} = cos(\phi)\hat{y} - sin(\phi)\hat{z}. \tag{2.33}$$

The velocity-aligned coordinates are useful because we can eliminate the velocity dependence on ϕ by applying following rotation matrix

$$\begin{bmatrix} \hat{x'} \\ \hat{y'} \\ \hat{z'} \end{bmatrix} = \begin{bmatrix} 1 & 0 & 0 \\ 0 & sin\phi & cos\phi \\ 0 & -cos\phi & sin\phi \end{bmatrix} \begin{bmatrix} \hat{x} \\ \hat{y} \\ \hat{z} \end{bmatrix} \tag{2.34}$$

Keeping the x-axis the same, the velocity vector is now aligned but in opposite direction with the new z-axis. The velocity of the hot spot aligns with the new z axis but in opposite direction

$$\hat{v} = -\hat{z'}. \tag{2.35}$$

Since the velocity vector is perpendicular to the position vector of the hot spot, the hot spot vector is simply made of two components

$$\hat{r} = cos(\theta)\hat{x'} + sin(\theta)\hat{y'}. \tag{2.36}$$

Using Equation 2.24, we can find $\hat{k_0}$ by from its dependence on $\hat{k}$ and $\hat{r}$

$$\hat{k_0} = \frac{1}{sin(\psi)}(sin(\alpha)\hat{k} + sin(\psi - \alpha)\hat{r}). \tag{2.37}$$

In the velocity-aligned coordinates, expanding the $\hat{k_0}$ dependence gives

$$\begin{aligned} \hat{k_0} = ((&sin(\alpha)cos(i) + sin(\psi - \alpha)cos(\theta))\hat{x'} \\ &+ (sin(\alpha)sin(i)sin(\theta) + sin(\psi - \alpha)sin(\theta))\hat{y'} + sin(\alpha)sin(i)sin(\phi)\hat{z'}), \end{aligned} \tag{2.38}$$

and expanding the dot product between $\hat{k_0}$ and v gives the final $cos(\xi)$

$$cos(\xi) = \hat{k_0} \cdot \hat{v} = -\frac{sin(\alpha)sin(i)sin(\phi)}{sin(\psi)}. \tag{2.39}$$

For a photon observed at E, its initial energy E_0 is subjected to Doppler shift and gravitational redshift

$$E/E_0 = \frac{\sqrt{(1 - r_g/R)}}{\delta}. \tag{2.40}$$

Since the quantity I_ν/ν^3 is Lorentz invariant, I_ν changes if ν changes along a photon path. There are three ways the Special Relativity affects the intensity profiles via Lorentz invariance: the photon's individual energy is modified; the emission angle to surface normal is Doppler shifted; the intensity values themselves are also modified via the ν^3 term in the denominator.

2.3.5 Total energy flux contribution

Combining the relativity effect on the hot spot's solid angle and intensity profiles, we obtain the energy flux formula

$$\begin{aligned} dF_E &= I d\Omega \\ &= (1 - r_g/R)^{3/2}\delta^3 I\Big(\frac{E}{\delta\sqrt{(1 - r_g/R)}}, cos(\alpha)\delta\Big)\frac{R^2}{D^2}\frac{1}{1 - r_g/R}cos(\alpha)\delta\frac{dcos(\alpha)}{dcos(\psi)}dcos(\psi)d\varphi. \end{aligned} \tag{2.41}$$

We can calculate the total energy flux based on the differential, but photon flux is of more importance due to the nature of X-ray detectors. To do so, we can either divide the differential by energy per photon, or use the result from section 2.1 for a quick integration method that uses the log-spaced energy grid of the intensity profile.

2.3.6 The Oblate-shaped Neutron Star

Neutron stars are not rigid bodies; the faster one spins, the more oblate its surface gets. The formulation described in the previous section is known as Schwarzschild plus Doppler approximation, which assume the surface is a

sphere. This first-order approximation is correct for a spherical NS. A simple approximation scheme known as the Oblate Schwarzschild approximation (Morsink et al., 2007) allows for the correct oblate shape of the NS to be included. In addition, the oblate structure changes the distance from the NS centre to the surface, depending on latitude, thus surface gravity changes with latitude as well. Effective gravity on the surface of a fast-spinning NS is also reduced slightly by the centrifugal force. We adapt the correction formula for effective surface gravity as derived by AlGendy and Morsink (2014). The rotation parameter is defined as

$$\bar{\Omega} = \Omega\Big(\frac{R_e^3}{GM}\Big)^{1/2}, \tag{2.42}$$

where Ω is the angular speed of the rotation, R_e is the equatorial radius, and M is mass of the NS. The full correction ratio is normalized to the surface gravity for a non-rotating NS using its equatorial radius g_0

$$g_0 = \frac{GM}{R_e^2}\frac{1}{\sqrt{1-\frac{2GM}{R_e}}}, \tag{2.43}$$

$$\frac{g(\theta)}{g_0} = (1 + c_e\bar{\Omega}^2 sin^2(\theta) + c_p\bar{\Omega}^2 cos^2(\theta)), \tag{2.44}$$

where the coefficients c_e and c_p depend on compactness of the NS (AlGendy and Morsink, 2014). The NS atmosphere structure is influenced by the gravity via hydrostatic equilibrium. By considering the oblate shape of the NS in our work, we follow the formulation known as Oblate Schwarzschild approximation. The formulation ensures the inclusion of oblate correction, and is especially important when considering fast-spinning NS such as the millisecond pulsars.

2.4 Processing of Signals from NS to Detection

For a photon to be recorded by a telescope, it must travel from the source, through the ISM, and interact with the detector within its effective collecting area. The ISM attenuates the X-ray photons by scattering them out of the telescope's line of sight, causing the photon flux to decrease. The collection plates of the telescopes interact with photons when they reach the Earth. Depending on the designs, the physical sizes, and the efficiencies of the telescopes, the effective areas depend on photon energies and telescope designs. Out of the differential components associated with the specific intensity, we have so far covered strategies in integrating frequency/energy and solid angle. The final two steps, collecting area and observation time, are integrated to obtain the final counts. In this section, we discuss the modelling of the final components in the waveform as received by telescopes, specifically *NICER*'s observation of PSRJ0437 and its surrounding sources.

The final tally of photons are the sum of the contribution from the NS and its nearby sources, and are subjected to scattering and absorption processes between the sources and the Earth. Since *NICER* is not designed to concentrate X-ray photons, its large field of view contains other nearby sources when observing the neutron stars. We classify components of the photons into two kinds: phase-dependent signals originating from PSRJ0437, the primary target of *NICER*, and a phase-independent background, which includes an Active Galactic Nucleus (AGN) of a nearby Seyfert galaxy RX J0437.4-4711 (Wang et al., 1998), unresolved background sources, and sources on the International Space Station (ISS).

The signals, pulsed or unpulsed, are subjected to different effects depending on their origin. Earlier observations by *XMM-Newton* and *NuStar* telescopes suggest that the phase-dependent signals have two hot spot NS atmosphere components and a power law component (Bogdanov et al., 2007; Guillot et al.,

2016). The AGN of RX J0437.4-4711 (Wang et al., 1998) contributes to a phase-independent power law background. These three sources are subjected to the attenuation by the Interstellar Medium (ISM). The remaining unresolved sources in *NICER*'s field of view while observing targets are grouped together as "diffuse sky". In practice, we measure the unresolved sources after the ISM attenuation, so this component is grouped with photons from modules of the International Space Station. All of the photons are also subjected to the response matrix of *NICER*'s detectors, and the total effective area varies with photon energy. We will produce the composite waveform templates based on the components from the NS hot spot, the phase-dependent power law, the AGN, and the measured diffuse sky signals.

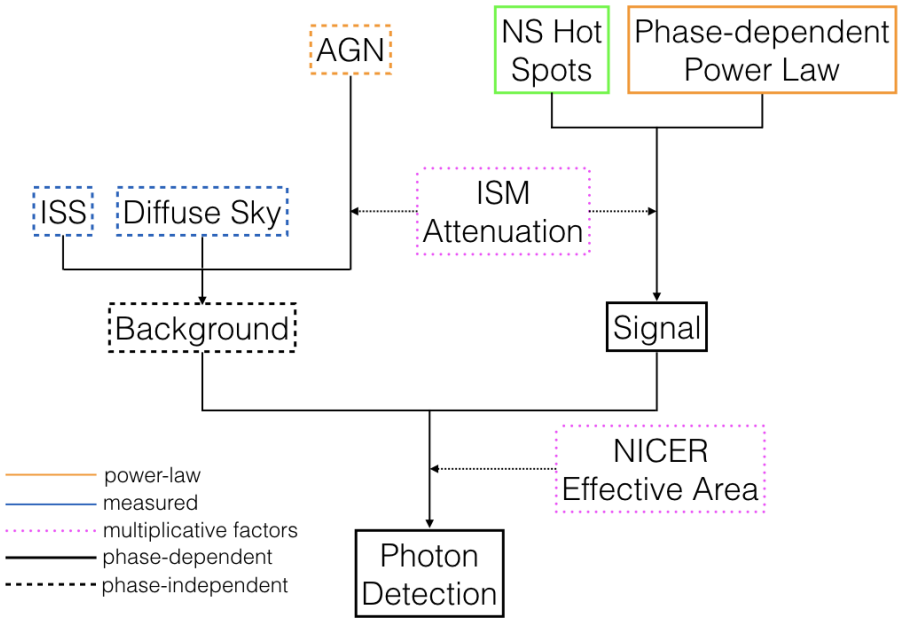

Figure 2.7: The final photon counts are consisted of various signal and background components.

2.4.1 RX J0437.4-4711

The proximity of Seyfert I galaxy RX J0437.4-4711 near PSRJ0437 makes it fall within *NICER*'s field of view. The origin of the soft X-ray photons is the AGN

at the centre of the galaxy. A power-law model with photon index $\Gamma = 2.59$ can be used to describe *ROSAT* observation on the galaxy (Wang et al., 1998). The power-law model has the form

$$p(E_0) = A(E_0)^{\Gamma} dE, \tag{2.45}$$

where p is the photon flux, A is the normalization factor, E_0 is the photon energy of the centre of the energy bin, and dE is the width of the energy bin. However, the model does not consider mechanisms such as Comptonization and metal K lines and the long term variability of the AGN. Moreover, the single component power-law does not describe potential spectral complexity. We use this crude approximation only to account for most of the phase-independent background.

2.4.2 Phase-dependent Power Law Component

A pulsed emission at high energies originating from PSRJ0437 was observed by *NuStar*. This observation has been phenomenologically described as a power law (Guillot et al., 2016). Possible origins of the power-law tail are magnetospheric emission processes and weak Comptonization (Bogdanov et al., 2007), which are not directly related with the surface hot spots. Even though this component was treated as a constant source in the early works, *NICER*'s long observation will accumulate a significant amount of photons contributed by this component. The *NuSTAR* observation by Guillot et al. (2016) suggested that the power law component is likely pulsed, although the low number of counts by the *NuSTAR* observation can't confirm this due to low signal-to-noise ratio. Even though the power law contribution to the overall source count is greater than the thermal component at above 3keV (Guillot et al., 2016), the weak power-law tail is not expected to be a major contributor to the background, accounting for only 5-10% of the total counts given *NICER*'s response curve.

We do not cover the modelling of the phase-dependent power law component in this project, albeit it should be included in future works, since the component will increase photon counts at higher energies, causing bias in the radii estimate.

2.4.3 ISM Attenuation

As photons passes through the ISM, a portion of them interact with the ISM and are lost along the path to the observer. In this thesis work, we adapt the model *TBnew*, which is a variant of the ISM attenuation model by Wilms et al. (2000). The total attenuation cross section of the interstellar medium is contributed by cross sections of the gas, molecules, and dust grains components

$$\sigma_{ISM} = \sigma_{gas} + \sigma_{molecules} + \sigma_{grains}. \tag{2.46}$$

The attenuation factors depend on the photon energies. The cross sections decrease in general with higher energies, except at jumps created by additional K edge energies of elements. The abundance of elements in the ISM should be set to the suggested values in this paper, instead of older values by Anders and Grevesse (1989). The cross sections are normalized to the total hydrogen column density N_H

$$I_{obs}(E) = e^{-\sigma_{ISM} N_H} I_{source}(E). \tag{2.47}$$

The *TBnew* model is available via the spectral fitting tool XSPEC as an ISM attenuation model. We obtained a copy of the attenuation factors normalized to $N_H = 4 * 10^{19} cm^{-2}$. The factors can be calculated for any hydrogen column density by using the formula

$$f(E, N_H) = f(E, 4 * 10^{19} cm^{-2})^n, \tag{2.48}$$

$$n = \frac{N_H}{4 * 10^{19} cm^{-2}}. \tag{2.49}$$

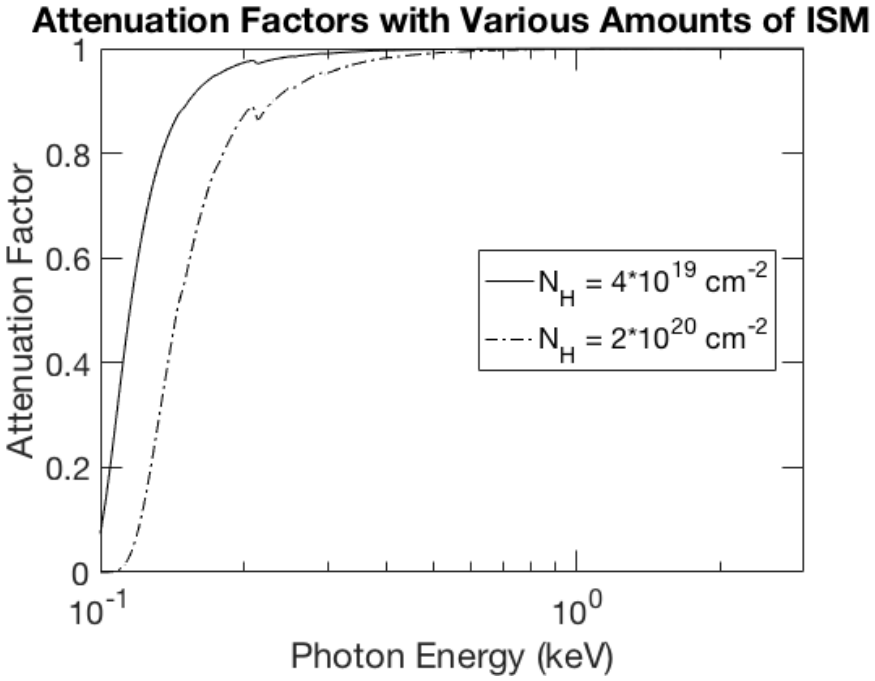

Figure 2.8: ISM attenuation factors depends on hydrogen column density.

We apply the attenuation factors to the affected signals before combining them with the diffuse sky in the next step.

2.4.4 Effective Areas of *NICER*

Folding the photon flux against the response matrix of *NICER* produces the final photon count rates. The response matrix describes the effective areas of *NICER*'s channels dependence on photon energy. *NICER* has 1191 channels, and each channel is sensitive to photons in an energy range. Thus for photons at the same energy, they would be detected by several channels, each with an effective area. For example, there are 33 channels with non-zero effective areas for photons with energy at 0.3 keV. Thus the final photon counts for each energy band is a result of folding the intrinsic photons with the response

matrix.

Previous efforts determined that photon counts in the range of 1 million is needed to achieve a 5% constraint in the mass-radius relation (Bogdanov et al., 2007). From the expected photon flux of PSRJ0437, sensitivity near 0.3 keV should be optimized. With current design limits, the peak effective area should be at least $1333cm^2$ at 1 keV. The peak effective area of *NICER* is just shy of $2000cm^2$, and is designed so that significant amount of photons can be recorded for observing three targets at 1.5 million seconds each (Arzoumanian et al., 2014). We obtained an response curve of *NICER* from ground testing, and its properties will be understood better after the calibration process.

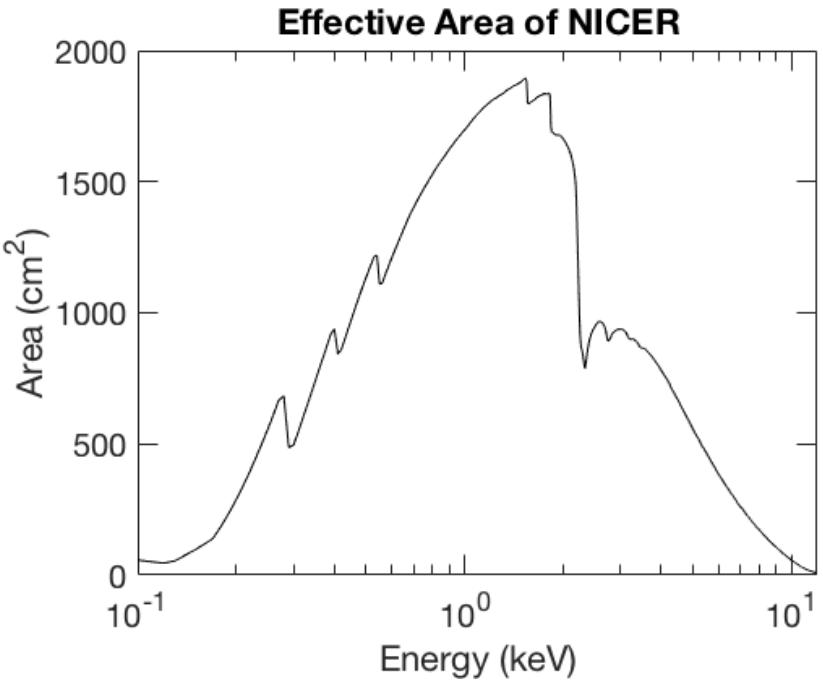

Figure 2.9: *NICER*'s effective area changes with photon energy.

2.4.5 Signal Management

The total count rate for *NICER*'s observation in the field of PSRJ0437 will be in the order of 1 count/second. The waveform contributions can be split into two general fields: phase-dependent and phase-independent. For the phase-

independent component, we expect 0.4 counts/second from the AGN and 0.3 counts/second from the diffuse sky. In the phase-dependent component, most of the photons are from the hot spots on the NS, and the expected rate of 0.03 counts/second by the power-law tail is small when compared with the overall pulse shape. The count rates from each components are not fixed values, but they will not be problematic because the majority of the background is either phase-independent or small compared with the actual signals by NS hot spots.

Chapter 3

Neutron Star Atmosphere Models

To understand the properties of the atmosphere models, we conduct a series of tests on the interpolation of the intensity profiles. We obtained the latest version of NSX Hydrogen (Ho, 2017) atmosphere intensity profiles that will be used by *NICER* science team for the light curve analysis. First, we test the interpolation properties by using linear, exponential, and power law schemes from the nearest two values of temperature, surface gravity, and emission angle to the surface normal. We find where the greatest errors in interpolation occur for interpolating to different temperatures. Second, for interpolating in photon energy, we test the difference between two- and four-point interpolation. Finally, we compare the difference in intensity profiles between the NSX models and the McPHAC hydrogen model. Understanding the properties of the atmosphere models paves the way for modelling light curve of rotation-powered X-ray MSPs.

3.1 Format of the Intensity Profiles

The intensity profiles are available as a function of temperature, surface gravity, emission angle to the surface normal (α), and energy. NSX Hydrogen models have logarithmically-spaced grids for temperature, surface gravity, and energy, while emission angle to the surface normal is equally-spaced in α with special spacings between the first five and the last five grid points. Table 3.1 shows the parameters of the available intensity profiles for NSX Hydrogen.

Variable	Minimum	Increment	Maximum	Number of Grid Points
Temperature (K)	$10^{5.1}$	$10^{0.1}$	$10^{6.5}$	15
Surface Gravity (cgs unit)	$10^{13.7}$	$10^{0.1}$	$10^{14.7}$	11
Energy (keV)	$10^{-1.32}$	$10^{0.02}$	$10^{1.4}$	137
α	0	$(\pi/120)^*$	$\pi/2$	67

Table 3.1: Ranges and number of grid points for essential variables in NSX Hydrogen model

McPHAC hydrogen models are available in similar style with some minor differences. The temperature grid is twice as dense as the NSX Hydrogen grid; the surface gravity is the same as the NSX Hydrogen grid; the energy grid is logarithmically-spaced in a normalized parameter of $\frac{h\nu}{kT}$, where h is Planck constant, ν is the frequency of the photon, k is Boltzmann constant, and T is the temperature; the emission angle is equally-spaced in α, and starting/ending points are not at exactly surface normal/surface parallel. Table 3.2 shows the parameters of the available intensity profiles for McPHAC Hydrogen.

Variable	Minimum	Increment	Maximum	Number of Grid Points
Temperature (K)	$10^{5.1}$	$10^{0.05}$	$10^{6.5}$	15
Surface Gravity (cgs unit)	$10^{13.7}$	$10^{0.1}$	$10^{14.7}$	11
$\frac{h\nu}{kT}$	$10^{-1.304}$	$10^{0.338}$	$10^{2.043}$	100
α	acos(0.015629)	0.031	acos(0.999710)	50

Table 3.2: Ranges and number of grid points for essential variables in McPHAC hydrogen model

Since NSX Hydrogen uses the same energy grid for all intensity profiles, we can interpolate between all choices of temperature, surface gravity, and α directly as a function of energy. We examine the properties of NSX Hydrogen profiles in the next sections.

3.2 Interpolation: Three Methods on Three Parameters

3.2.1 Temperature

As described in the introduction section 1.5, the NS atmosphere is generally assumed to be in local thermal equilibrium. The emergent intensity profiles are thus thermal in nature. Temperature has the greatest effect on the thermal intensity profiles. For the purpose of demonstration, we choose the conventional case of surface gravity log(g) = 14.2 and only consider the case where the emission is normal to the surface. Figure 3.1 shows the example NSX Hydrogen intensity profiles with various temperature.

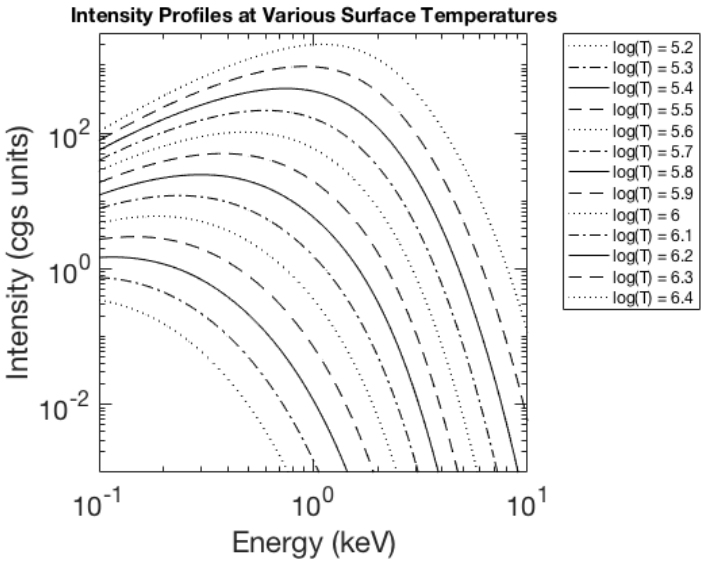

Figure 3.1: The intensity profiles are Planck-like and strongly dependent on temperature

To determine which of the three schemes, linear, exponential law, and power law, is the best, we fix the surface gravity to log(g) = 14.2, emission to normal to the surface and, interpolate the intensity profiles by using the known values on the temperature grid. Since the temperature grid has the increment of log(T) = 0.1 between the 15 values, we can interpolate the 13 intermediate temperature values using the known profiles from the neighboring temperature values. For example, we would use the profiles of log(T) = 5.9 and log(T) = 6.1 to interpolate log(T) = 6. There are 137 photon energy points for the intensity profiles, so there are 137 degrees of freedom. We calculate the χ^2 values between the known and the interpolated intensity profiles with the formula

$$\chi^2 = \sum_{j=1}^{137} \frac{(k_j - i_j)^2}{k_j}, \tag{3.1}$$

where k_j and i_j are the known and interpolated intensity values at the jth photon energy, respectively. Note that this is not the standard χ^2 formula used in statistics, since we use scale the contribution of each data point by k_j instead of the standard error. We use this formula to quantify the goodness

of our interpolations. Figure 3.2 shows the χ^2 values per degree of freedom of each interpolation scheme.

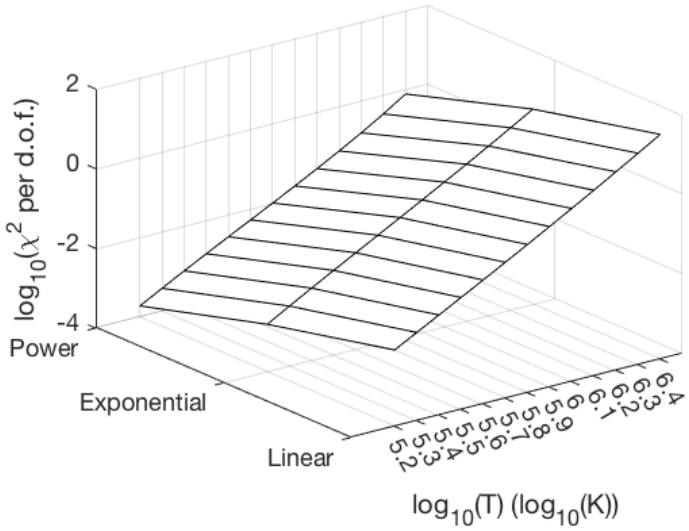

Figure 3.2: The power law scheme consistently produces the lowest χ^2 per degrees of freedom of the three schemes.

The χ^2 values per degree of freedom are always the smallest and below 1 for all temperature interpolated to by using the power law scheme. We calculate the difference between actual and interpolated intensity profiles, and find the photon energy of maximum errors, E_{max_e}. The result is shown in Figure 3.3.

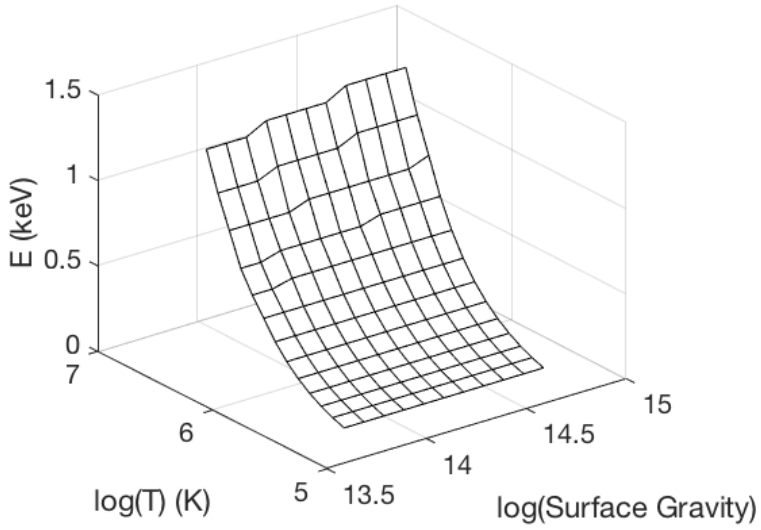

Figure 3.3: Photon energy of maximum errors E_{max_e}, given a specific set of surface temperature and gravity. E_{max_e} increases with both temperature and gravity, and occurs at roughly the photon energy of peak intensity.

As temperature increases, the photon energy at peak intensity also increases due to thermal nature of the emission. The greatest interpolation error thus occurs near the peak. Even though the maximum difference in intensity increases with temperature, the errors never exceed 5%. Future works will identify alternative interpolation methods in order to reduce the errors. The specific maximum error percentage is shown in Table 3.3.

Temp. (log(K))	Temp. (keV)	E_{max_e} (keV)	Max (%) Difference in Intensity
5.2	0.014	0.100	-4.52
5.3	0.017	0.126	-4.49
5.4	0.021	0.159	-4.43
5.5	0.027	0.200	-4.36
5.6	0.034	0.251	-4.30
5.7	0.043	0.316	-4.28
5.8	0.054	0.398	-4.21
5.9	0.068	0.501	-4.21
6	0.086	0.631	-4.23
6.1	0.11	0.759	-4.20
6.2	0.14	0.955	-4.28
6.3	0.17	1.15	-4.37
6.4	0.22	1.38	-4.60

Table 3.3: Power law interpolation error in intensity, for profiles of log(g) = 14.2 at various temperatures.

Figures 3.4 and 3.5 show the interpolations at the highest and the lowest temperatures. The upper subplots show the intensity profiles of the nearby temperature in dashes, while known and interpolated profiles are in solid lines of different colors. The power law scheme produces interpolations that are closest to the known values. The lower subplots show the differences between power law interpolations and the known values. These figures reinforces the idea that maximum error occurs near the photon energy of peak intensity.

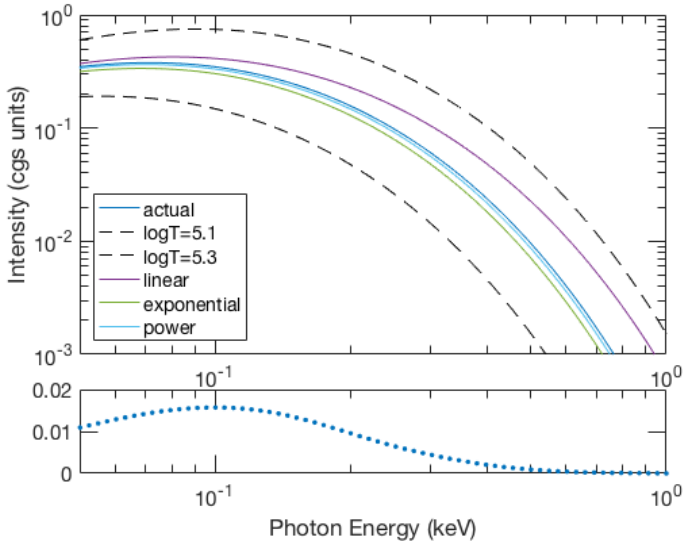

Figure 3.4: The upper panel shows the interpolations via the three schemes. The linear scheme is skewed by the profile of log(T) = 5.3, while the exponential scheme underestimates the intensities. The lower panel shows E_{max_e} of log(T) = 5.2 is near 0.1 keV for power law scheme.

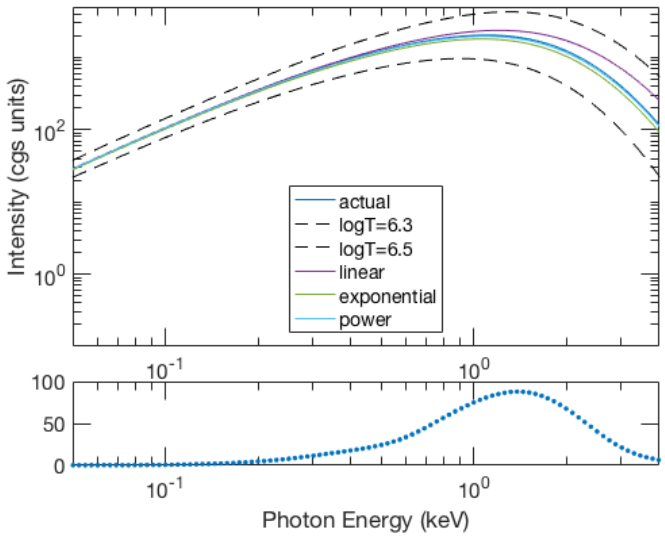

Figure 3.5: Similar to Figure 3.4, the upper panel shows the interpolations via the three schemes and the lower panel shows E_{max_e} of log(T) = 5.2 for power law interpolation. E_{max_e} of log(T) = 5.2 is near 15 keV for power law scheme.

3.2.2 Surface Gravity

The surface gravity affects the structure of the atmosphere models via hydrostatic equilibrium. However, the effect on the intensity profiles is small when compared with the effect of temperature. The increased gravity slightly reduces the peak specific intensity and increases the specific intensity in the high energy tail. Figure 3.6 shows the effect of surface gravity on the intensity profiles.

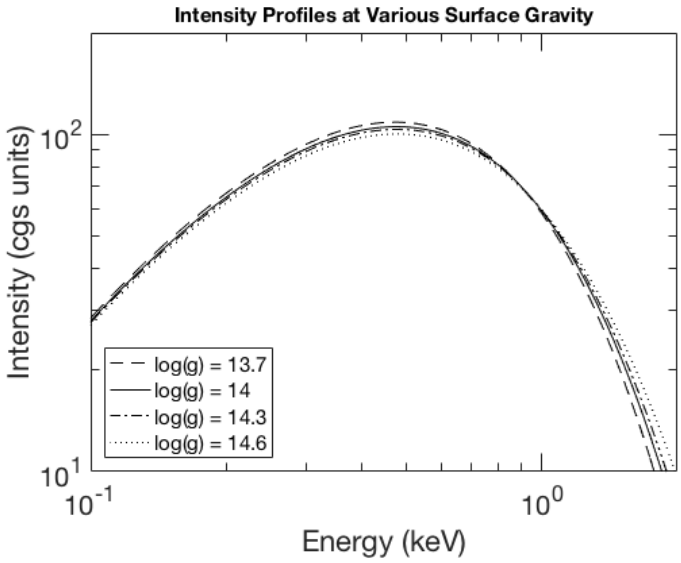

Figure 3.6: The intensity profiles is slightly flattened with increasing surface gravity.

The interpolated profiles have very small differences compared with given profiles. The χ^2 values per degree of freedom is < 0.02 for all of the models. Even though all three methods give small χ^2 values, the χ^2 values for the power law scheme are consistently the smallest of all three schemes.

3.2.3 Emission Angle to the Surface Normal

The dense angle grid shows that interpolation errors for the emission angle are very small. For the case of surface temperature log(T) = 6 and surface gravity log(g) = 14.2, the χ^2 values per degree of freedom is less than 0.05 for $cos(\alpha) > 0.0262$. The intensity profiles behaves non-linearly for emission

near surface parallel, but their contribution to the overall light curve is almost negligible. We do not expect significant interpolation errors from the emission angle.

3.2.4 Two-point vs Four-point for Energy

To find the specific intensity value at a photon energy, we interpolate from the atmosphere energy grid. Curvature exists in the intensity profiles since they turn over at higher energy. We compare the simple cases of using two points to interpolate under the three schemes (linear, exponential, and power) with using four-point polynomial under the three schemes to investigate the need for using more data points. We fix the number of free parameters to 2 to ensure consistency. Figure 3.7 shows the two- and four-point interpolated profiles of log(T) = 6, log(g) = 14.2, and cos(α) = 1 using power law scheme.

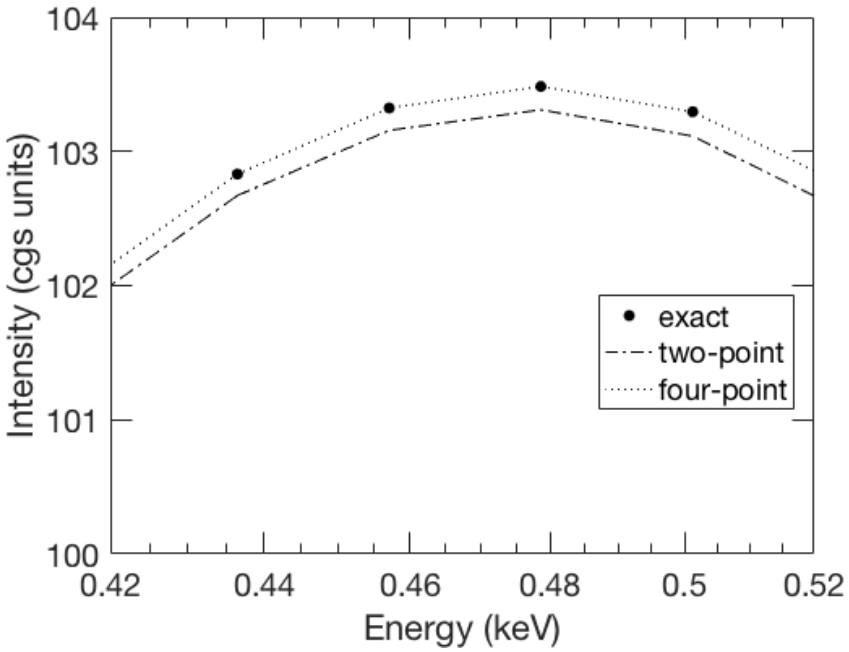

Figure 3.7: Two-point and Four-point power law interpolation with respect to photon energy. Two-point interpolation consistently produces larger errors.

The linear and exponential law schemes show virtually no difference to the

interpolated results, but the two-point interpolations always underestimate the intensity near the peak. Although the χ^2 values presented in Table 3.4 are small, they are consistent with the implication that four-point interpolation is preferred over two-point interpolation.

	Linear	Exponential	Power
2-point	0.0666	0.0133	0.0192
4-point	< 0.0001	< 0.0001	< 0.0001

Table 3.4: χ^2 values of each interpolation scheme for two- or four-point with respect to photon energy

The power law scheme works best for both cases of two and four data points. Even though the difference is not significant, we choose to use four energy points for interpolation to achieve the highest accuracy.

3.2.5 Comparison of Intensity Profiles

The intensity profiles of the atmosphere models follow a Planck-like curve; they are thermal in nature. To compare the differences in the atmosphere models, we examine them at different temperature while keeping the surface gravity constant. We already learned that the surface gravity dependence is much smaller than temperature dependence (see sections 3.2.1 and 3.2.2). NSX models are available in a wide variety of atmosphere compositions. Three NSX models of important compositions, fully-ionized hydrogen, partially-ionized hydrogen, and helium, are recently calculated to high-precision (Ho, 2017). For $T = 1.12 \times 10^6 K$ and log(g) = 14.2, the tables are fully-computed.

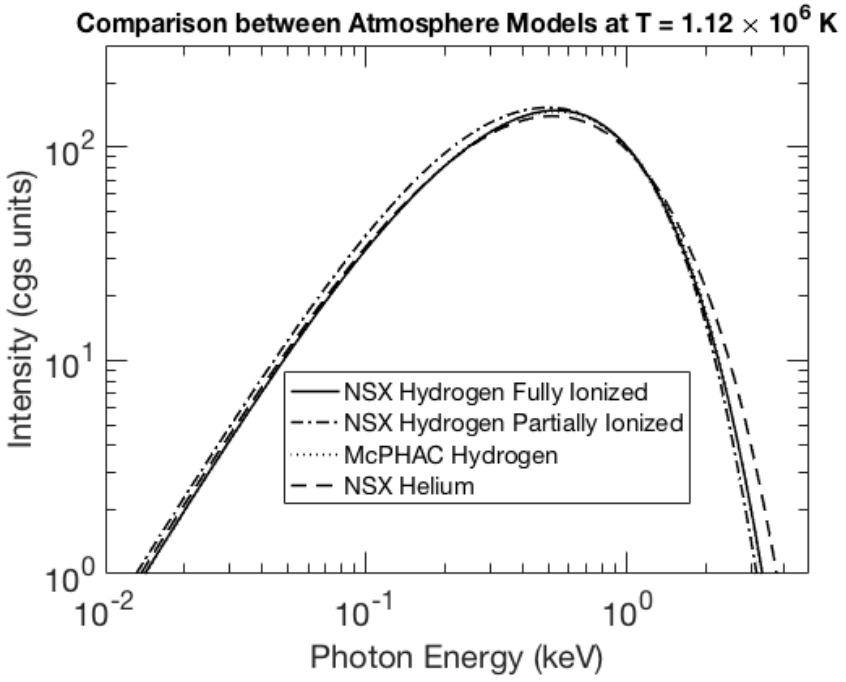

Figure 3.8: Comparison of Intensity Profiles at $T = 1.12 \times 10^6 K$. The difference between fully-ionized NSX Hydrogen and McPHAC Hydrogen models are barely noticeable. The partially-ionized NSX Hydrogen produces a softer profile, while NSX Helium produces a harder profile.

In Figure 3.8, we compare the intensity profiles between the NSX models and the McPHAC model. McPHAC hydrogen model produces almost completely identical profile to the NSX fully-ionized hydrogen model. Since both of them are independently constructed, it adds reliability that they produce the same results. The partially-ionized version of NSX is only available for $T = 1.12 \times 10^6 K$. The emergent intensity profiles are softer than the completely-ionized model produces. This is due to the weaker Thomson scattering with the partially-ionized hydrogen atmosphere. However, the absorption lines are not visible in this temperature, indicating that a significant amount of hydrogen atmosphere is fully-ionized. The helium model is flatter overall when compared with hydrogen atmosphere. This is due to the increased Thomson scattering, causing the redistribution of photons to higher energy. In particular, it is weaker than the hydrogen model between 0.25 and 1 keV and

stronger at energies above 1 keV.

Figure 3.9 shows the intensity profiles at $T = 4.90 \times 10^5 K$. The intensity profiles at $T = 4.90 \times 10^5 K$ are about one order of magnitude weaker than the profiles at $T = 1.12 \times 10^6 K$. This reflects the strong dependence of the intensity profiles with temperature. In addition, the helium model no longer has the stronger high-energy component, a result of the stronger temperature dependence of Thomson scattering.

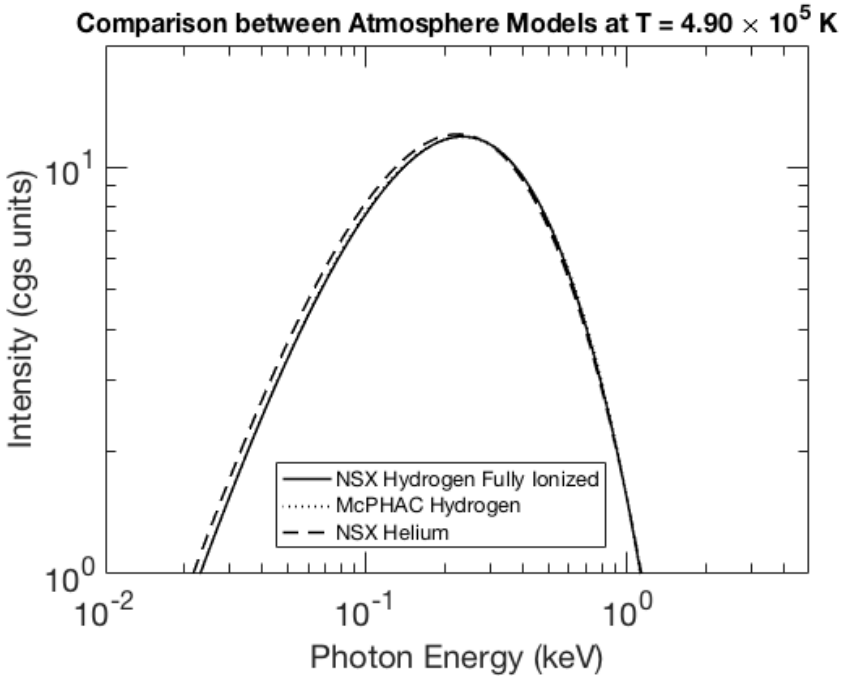

Figure 3.9: Comparison of Intensity Profiles at $T = 4.90 \times 10^5 K$

Figure 3.10 shows that at $T = 2.00 \times 10^6 K$, the intensity profiles are about one order of magnitude stronger than the profiles at $T = 1.12 \times 10^6 K$. The high energy tail is more easily-seen, further giving proof to the stronger Thomson scattering dependency on temperature for helium.

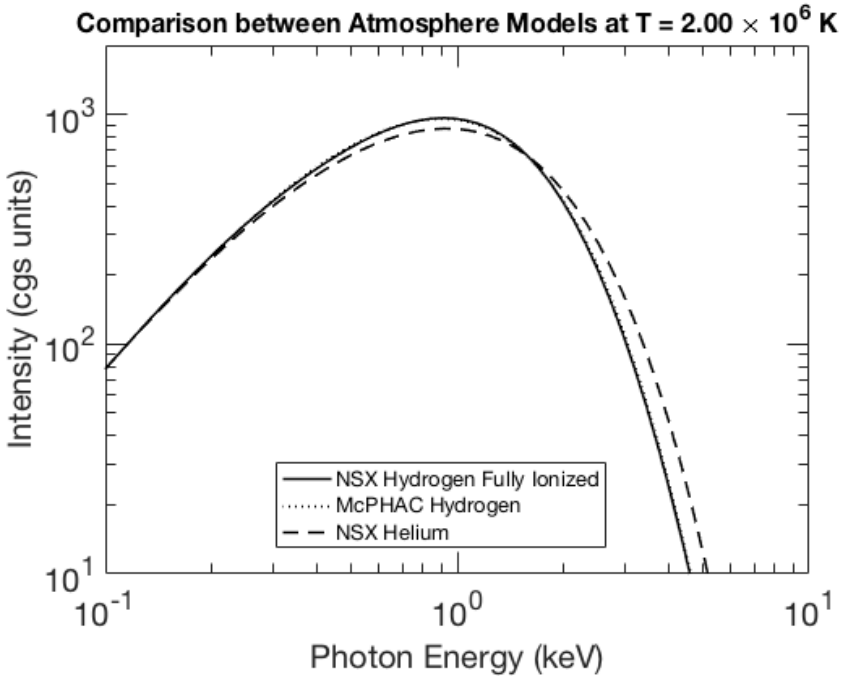

Figure 3.10: Comparison of Intensity Profiles at $T = 2.00 \times 10^6 K$

3.3 Chapter Summary

We have investigated the properties of the intensity profiles produced with different neutron star atmosphere models and compositions. We find that interpolating between the variable grids works best with the power-law scheme. We can use two-point interpolation for temperature, surface gravity, and emission angle, while four-point interpolation is needed for photon energy. The primary opacity source at this temperature is Thomson scattering, thus the helium atmosphere produces harder intensity profiles than the hydrogen atmosphere. The hydrogen models from NSX and McPHAC agree well with each other, adding credibility and consistency to the two models. We will make use of the atmosphere models to produce light curves in the next chapter.

Chapter 4

Light Curve: Spectra and Waveforms

The NS hot spot modelling program at the University of Alberta was originally developed by Coire Cadeau (2007), with major modifications by Sharon Morsink and Abigail Stevens (2013). The program currently calculates photon bending angle ψ with a unique solution, which means that it is limited to $|\psi| < \pi$. Highly compact NS with $\frac{Rc^2}{GM} < 3.52$ could have regions that are multiply imaged (Olausen, 2008). In this thesis project, routines are modified and/or added to the program. The atmosphere intensity routines are built on early adaptations by Khaled Elshamouty (2016) with newer models suitable for high-precision hot spot modelling. We create new routines for the integration of atmosphere models, background sources, and signal processing. Furthermore, we test the accuracy of the modelling program using an estimate on PSRJ0437 by Bogdanov et al. (2007), with updated values by Bogdanov (2013) and high precision measurement using radio pulsar timing on mass, inclination angle, and distance by Reardon et al. (2016).

We expect *NICER* to see the phase-dependent modulation of the waveform caused by NS hot spots. Modelling the synthetic light curves comparable to what we expect *NICER* to produce allows us to examine the effects of atmo-

sphere models, ISM absorption, instrument response curve, and other effects. In particular, the waveform is affected by the physical phenomenon such as Doppler Shift, light bending, and the oblate shape of fast-spinning NS. This chapter describes the parameters required in hot spot modelling, as well as two NS configurations we use to examine the effects.

4.1 Parameters

We classify the parameters used in NS light curve modelling into three categories: light curve settings, NS configuration, and signal processing. The light curve settings group contains the specification in which the modelling of the light curve is done. The NS configuration group contains parameters that are NS specific, including mass, radius, atmosphere models, hot spot positions, and others. The signal processing group contains other sources or modifiers of the light curve that are not related to the NS. Background, ISM, response curves belong in this group.

4.1.1 Light Curve Settings

Light curve settings include model parameters that are essential computationally. These parameters specify how the computation of the light curve is done, and can be adjusted in order to improve accuracy and to suit the observation.

The photons are grouped according to their energies. Grouping the photons by energy shows the physical nature of the emission. Since a NS emits most of its soft X-ray via its cooling surface, the emission is expected to be thermal, and should follow closely with the NS atmosphere models. In order to accurately use the highly energy-dependent effective areas of the *NICER* response curve, we recommend setting the lower and upper energy bounds to 0.095 and 3.105 keV, respectively, and use 301 bands to allow for 0.01 keV in bandwidth.

The photons are also grouped by their times of arrival. Photons accumu-

lated by the receivers are folded against the spin period of the pulsar to create a waveform. We normalize the phases by 2π so that the phase goes from 0 to 1 in one cycle. The waveform is split into a number of phase bins to show the modulation caused by the hot spots. Depending on which phase the current bin is, the orientation of the hot spots contribute to the accumulation of photons. In addition, physical effects that are phase-dependent, including Doppler Shift and light-bending, are calculated accordingly. We typically use powers of 2 as the number of phase bins to model the symmetry in the waveform.

Each hot spot occupies a finite space on the surface of the NS. The spot is cut into constant latitude bins. The number of latitude bins is specified by the user. Longitude bins are equivalent to phase bins. Each bin of latitude and longitude has a unique emission angle from the local surface normal. We use the same emission angle for the extent of the bin to approximate contribution from this bin. The more spot bins there are, the more accurate the waveform is. On the other hand, more calculation time is needed for more spot bins used.

The code also allows the user to choose the spectral type of the output light curve. The first mode allows the user to set a number of photon energy points and calculate the monochromatic photon flux. This is equivalent of doing integration in specific intensity over variables of dt and $d\Omega$, time and solid angle. Observation time is set as a parameter, and *NICER* observations are expected to be totaling on the order of 10^6 photons for each object; solid angle $d\Omega$ is calculated from distance and angular extent of the hot spot, which are in the NS Configuration group. This mode allows us to see how the intensity profiles of the atmosphere models affect the light curve without doing proper energy integration, and is useful for testing when implementing new atmosphere models. The second mode allows the user to calculate the integrated photon flux, which is done by integrating the monochromatic flux over the energy band specified. Integration over dA, the detector area, is done with a separate option that will be introduced in the signal processing section.

4.1.2 NS Configuration

NS configuration parameters include NS specific information. These options should be changed with different targets being observed, as well as testing different models of the NS.

Stellar object-specific parameters include mass, equatorial radius, spin frequency, distance, inclination angle to line of sight, and shape of the NS. The shape of the NS can be set to spherical or oblate, and the oblate approximation follows the formulation of AlGendy and Morsink (2014). Some of the parameters are known via binary interaction with its companions and/or observation in other electromagnetic bands.

Hot spot parameters include the option to model one or two hot spots, beaming model, sizes (ρ) and temperature (T) of the hot spots, colatitude of the spot centre (θ), and phase angle of the spot centre (ϕ) for the second spot (see Figure 2.6). Beaming model refers to the several atmosphere models and modified blackbody models. Each of the models have a different intensity profile and beaming pattern. My work focuses on the comparison between several hydrogen and helium models. The available choices are NSX fully-ionized hydrogen, NSX partially-ionized hydrogen, McPHAC hydrogen, and NSX helium. The size and temperature can be specified separately for each hot spot. The centre of the first hot spot is always set to phase zero ($\phi = 0$), and the second hot spot's position can be specified arbitrarily and is not assumed to be antipodal relative to the first. Options to use different hot spot shapes and temperature gradients are allocated, but currently only a circular spot with homogeneous temperature is available.

4.1.3 Signal Processing

Signal processing parameters include the background sources, ISM attenuation, and instrument response curve. The background sources are additive to the NS

atmosphere models, while the ISM and the instrument response are multiplicative. Most of the parameters are measured in the lead-up to the commissioning of *NICER* in preparation for the project.

We allow the user to specify the contributions from each background source separately. Each background source count rate is normalized to the expected number of photons per second in the soft X-ray range of 0.1-3.1 keV. The choice for the particular range is to minimize the effect of the possible phase-dependent power law background as reported by Guillot et al. (2016). The phase-dependent power law is expected at 0.03 counts per second in the 0.1-3.1 keV soft X-ray range, but we have yet to implement this component. The phase-independent component is largely contributed by the nearby Seyfert galaxy RX J0437.4-4711, which we use the power law index of $\Gamma = 2.59$ reported by Wang et al. (1998) and normalized to 0.4 counts expected per second. The unresolved diffuse sky emission of the PSRJ0437 field is previously measured and expected at 0.3 counts per second. We use the two simple components just to account for a significant portion of the phase-independent background for the synthetic waveform, because future estimate will treat the phase-independent background as a single component. The suggested parameters are simply measurements from previous studies. Measurements of these backgrounds should be updated when *NICER* begins its operational runs.

Two multiplicative parameters are the ISM attenuation factors and the *NICER* response curve. The ISM attenuation factors are pre-calculated for each energy band. We currently have only the *TBNew* model implemented for *NICER* energy bands, but tables of other ISM models can be added. The ISM models also require user input for the hydrogen column density. We calculate the ISM attenuation factors in the direction of PSRJ0437 with the hydrogen column density normalized to $4 \times 10^{19} cm^{-2}$ (see equations 2.48 and 2.49), so that the ISM attenuation factors can be calculated for a wider range of N_H. Previous measurements of N_H in the direction of PSRJ0437 was depen-

dent on spectral modelling and had large uncertainty (Bogdanov, 2013). The *NICER* response curve refers to the table of effective areas at different energy bands. This is the dA term in the integration from specific intensity to photon counts. We implemented the instrumental response curve of *NICER* obtained in ground testing from 2014, although updated version of the response curve can be implemented easily in the future. Since the multiplicative parameters are energy-dependent, they play an important role in the energy spectrum of *NICER* observations.

4.2 Effects of NS Parameters: A Toy Model

To demonstrate the effect of individual parameters, we use a toy model with typical NS parameters. The basic properties we use are listed in Table 4.1.

Parameter	Value
Mass	$1.4M_{\odot}$
Radius	10 km
Spin Frequency	200 Hz
Inclination Angle	90 degrees ($\pi/2$ radian)
Number of Hot Spots	1
Atmosphere Model	NSX hydrogen (fully-ionized)
Surface Temperature of Hot Spot	1.12×10^6 K
Angular Size of Hot Spot	0.1 radian
Emission Angle	90 degrees ($\pi/2$ radian)
Distance to NS	156.3 parsecs

Table 4.1: Basic settings for the toy NS

The specific observation properties are listed in Table 4.2.

Parameter	Value
Number of Energy Bands	301
Size of Energy Bands	0.01 keV
Energy Band Boundaries	0.095 to 3.105 keV
Observation Time	10^6 seconds
Background Contribution	None
ISM	None
Instrument Response Curve	$1cm^2$ at all energies

Table 4.2: Observation settings for the toy NS

4.2.1 Spin

If the NS is spinning at a higher frequency, Doppler boost will distort the waveform and the spectrum. Previous efforts by Cadeau et al. (2007); Morsink et al. (2007) showed that the waveform is significantly different between a non-spinning NS and an NS with spin frequency above 300 Hz. Here we compare the difference between 200 Hz and 600 Hz. Figure 4.1 shows that the waveform rises and falls asymmetrically, due to Doppler boost caused by special relativity via the invariant quantity I_ν/ν^3 (see Section 2.3.4). Figure 4.2 shows that the high-energy tail in the spectra is stronger for NS with a higher spin frequency because of the increased blue-shift by Doppler shift, similar to work done on rotational broadening of blackbody by Bauböck et al. (2015).

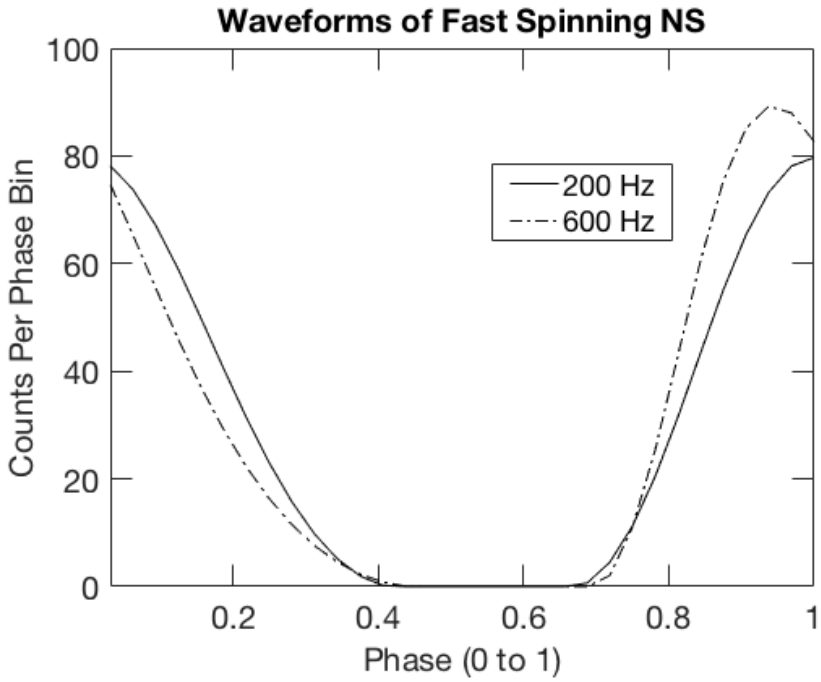

Figure 4.1: The waveform is distorted by the rapid rotation of the NS

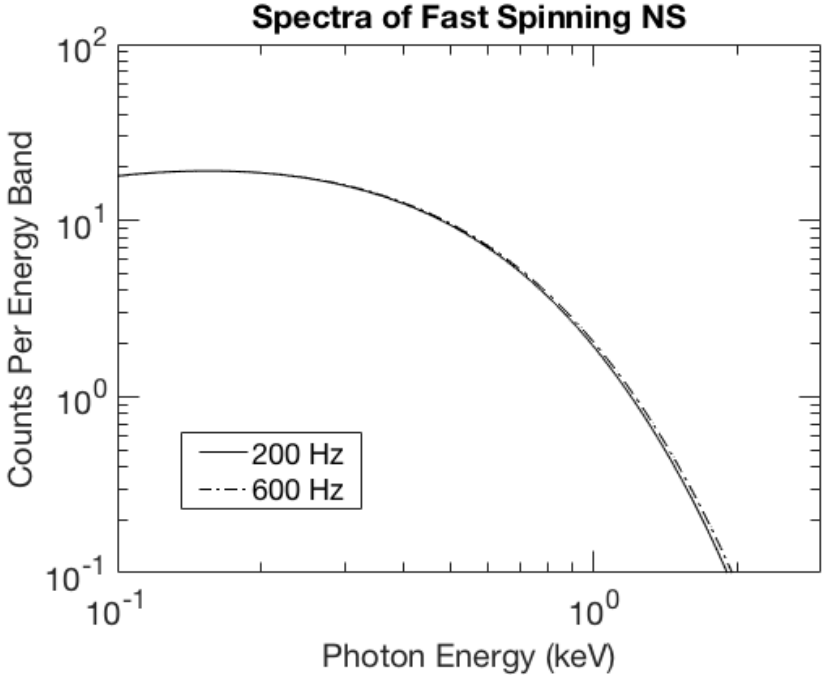

Figure 4.2: The spectrum is hardened by the Doppler boost

4.2.2 Temperature

The surface temperature affects the spectrum of the NS due to its thermal nature. Figure 4.3 shows the strong dependency of the spectra on the surface temperature. Figure 4.4 shows that the total numbers of photons follow the power law with respect to the surface temperature, which is expected from the form of Stefan-Boltzmann Law.

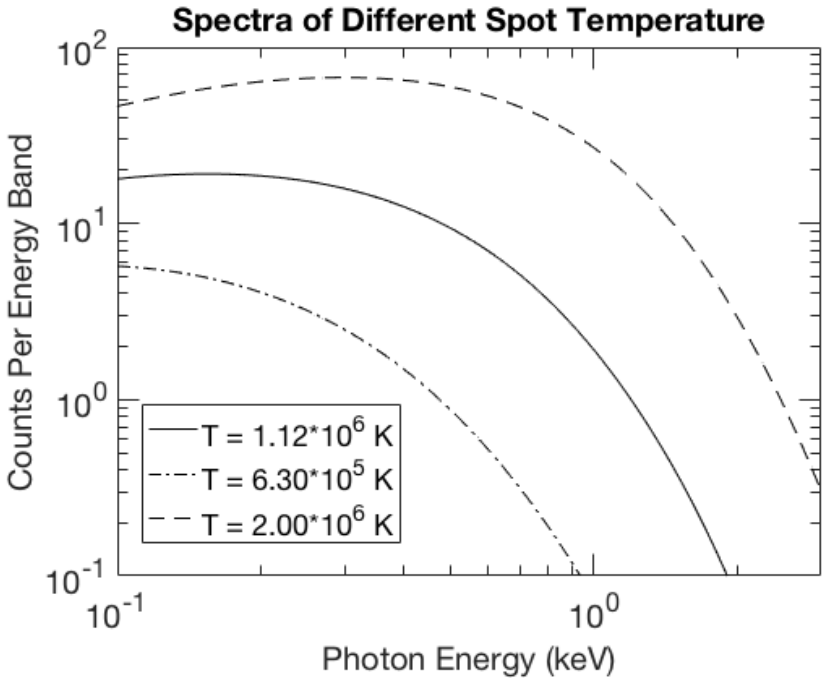

Figure 4.3: The spectra are Planck-like for their thermal nature.

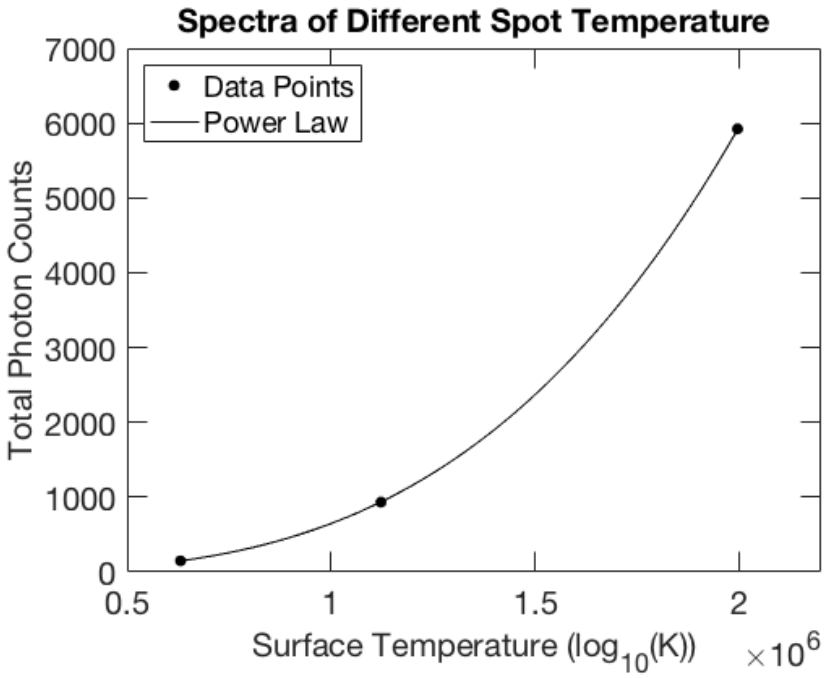

Figure 4.4: The total numbers of photons follow the power law with respect to the temperature.

4.2.3 Compactness

Increasing the mass while keeping the radius of the NS the same shows the effect of compactness of the waveform. Due to light-bending, the hot spot is visible even though it has gone beyond the Newtonian horizon. The increased compactness causes more light-bending, thus the X-ray eclipse is shorter. Figure 4.5 shows the shorter eclipse caused by the higher compactness of the NS.

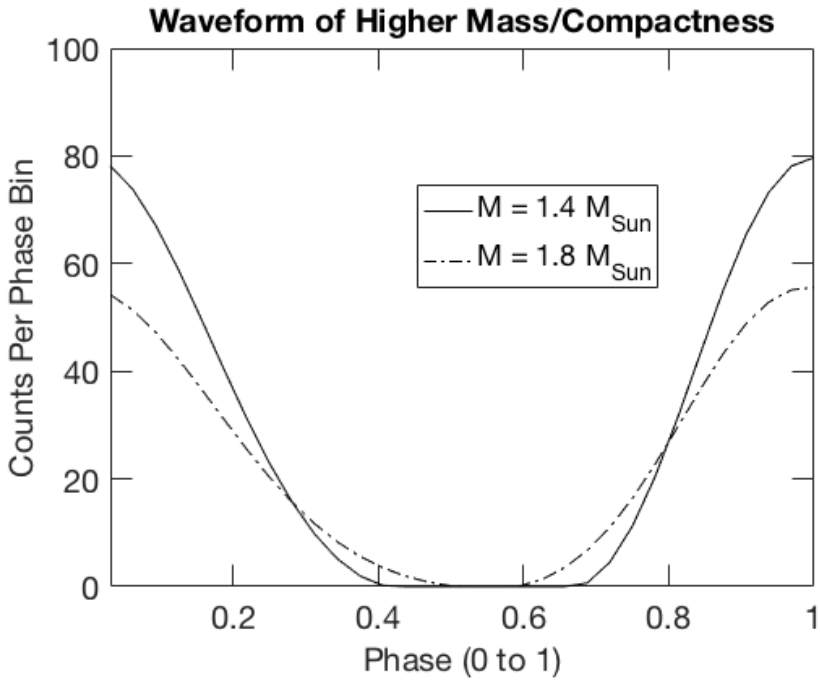

Figure 4.5: Higher compactness results in shorter eclipse

In addition, Figure 4.6 shows that the spectrum is more red-shifted due to the enhanced gravitational field.

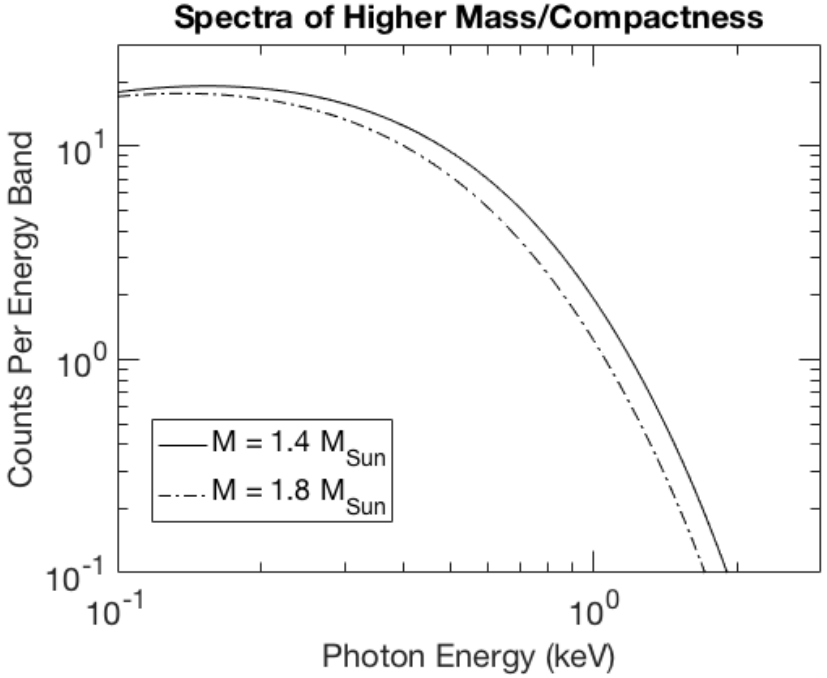

Figure 4.6: Higher compactness red-shifts the overall spectrum

4.2.4 Radius

To examine the effect caused solely by the NS radius on the light curve, we choose the mass and angular extent of the hot spot carefully so that the compactness and the emission area size remain the same. Figure 4.7 shows that keeping compactness constant while decreasing radius effectively increases the surface gravity.

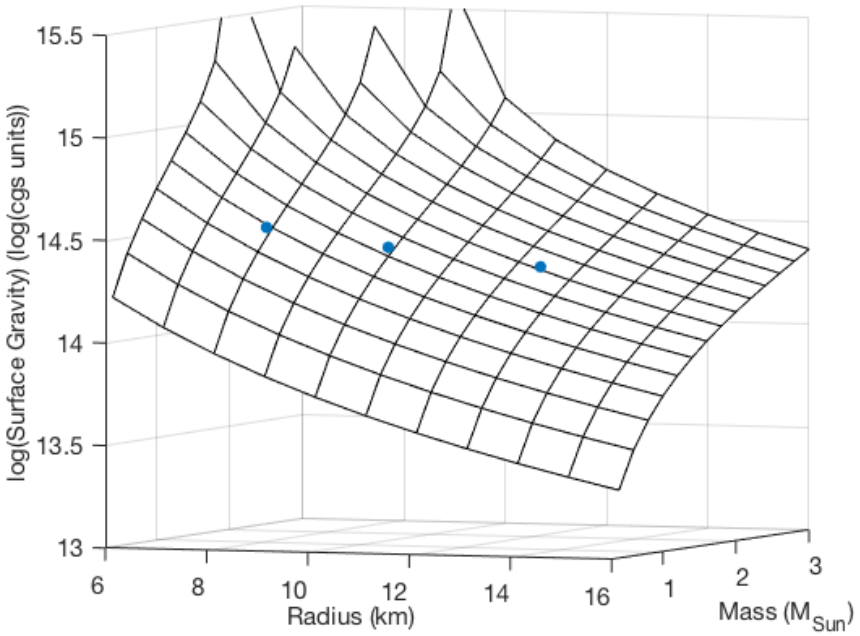

Figure 4.7: Surface gravity values at constant compactness. The smaller the radius is, the larger the surface gravity gets.

Figures 4.8 and 4.9 show that the small increase in surface gravity results in small increase in photon counts from the high-energy tail.

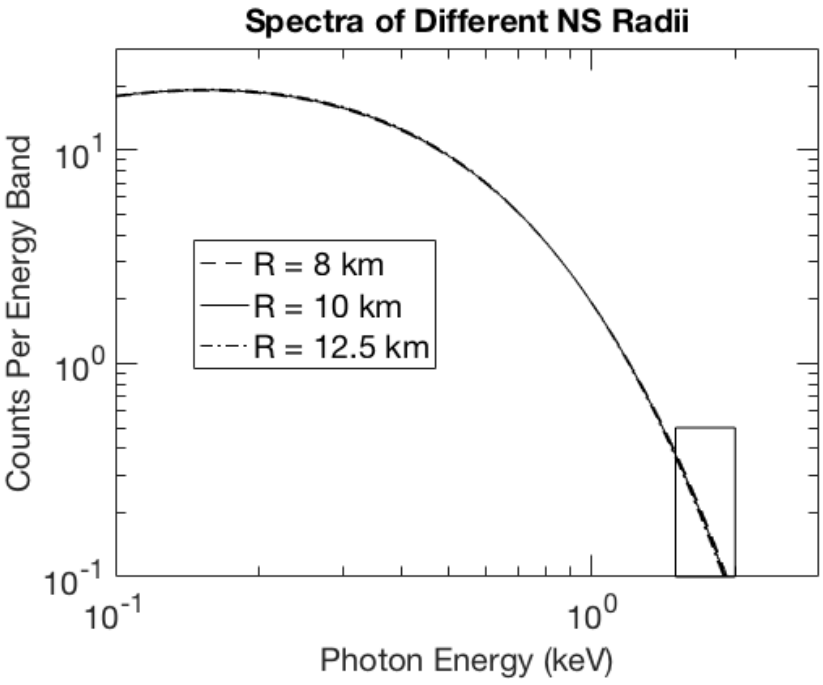

Figure 4.8: Seeing the small change requires zooming into the rectangular area in the figure.

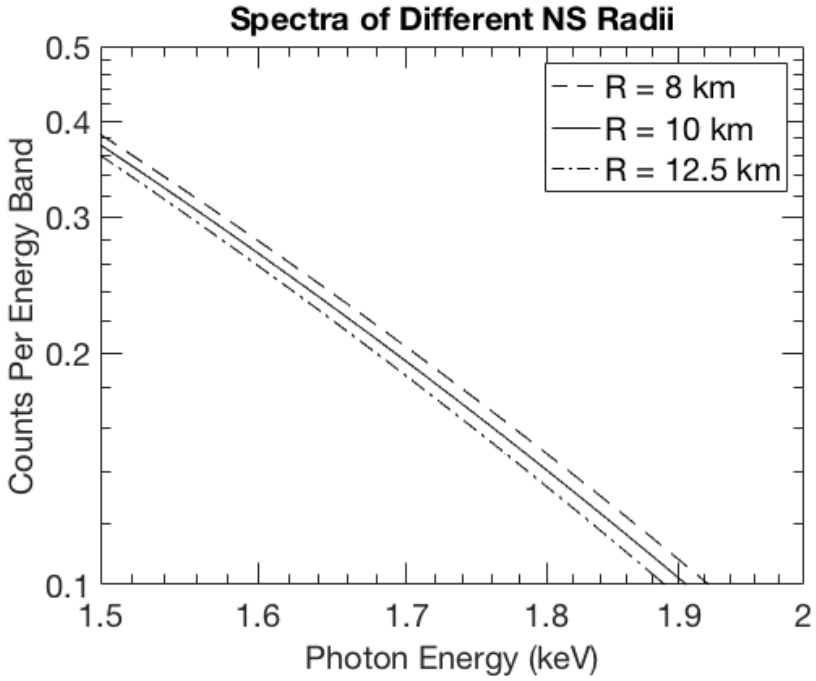

Figure 4.9: Influence of radius, thus surface gravity, on the observed spectrum. Decreasing the radius results in increases the surface gravity, which harden the high energy tail.

4.2.5 Second Spot

The surface hot spots do not always have the same temperatures or emitting areas. We add a second antipodal hot spot with a lower temperature and larger emitting area than the first hot spot. The second hot spot is $6.3 \times 10^5 K$ in temperature and 0.2 radian in angular radius. Figure 4.10 shows the waveform summed over all modelled energy bands. We can clearly see the contribution of the second hot spot creates the modulation near phase = 0.5. Due to its lower temperature, this hot spot contributes less photons.

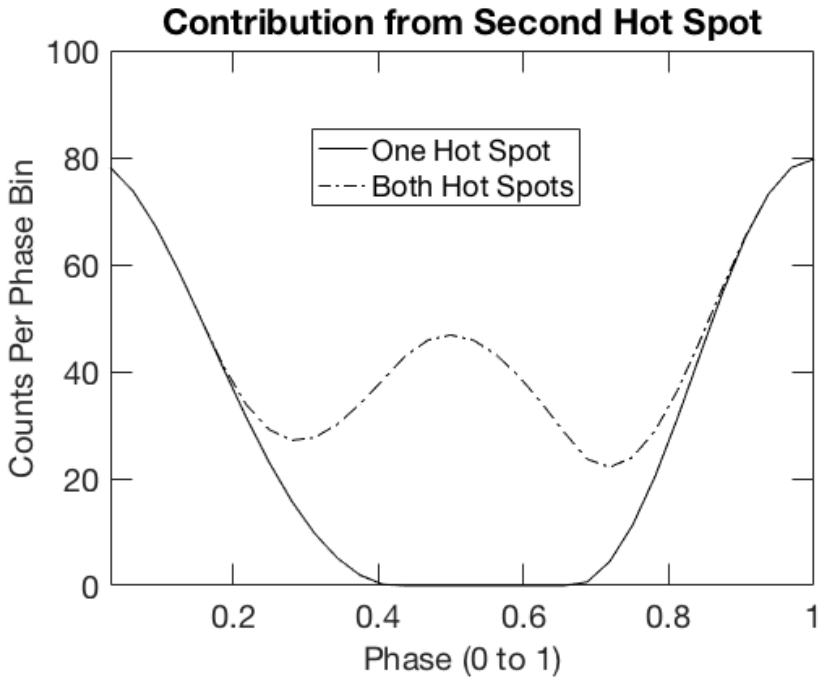

Figure 4.10: Waveform summed over all energies. Contribution by the second spot is located near phase = 0.5

The second hot spot's contribution also decreases more quickly than the first hot spot at higher energy. Figure 4.11 shows the waveform for the energy band from 0.195 to 0.205 keV. The two hot spots contribute to about the same amount of photons at this energy band. Figure 4.12 shows the waveform for the energy band from 1.995 to 2.005 keV. The second hot spot contributes minimally at this energy band. The diminished contribution by the second hot

spot at higher energies is the result of the thermal nature of the NS atmosphere.

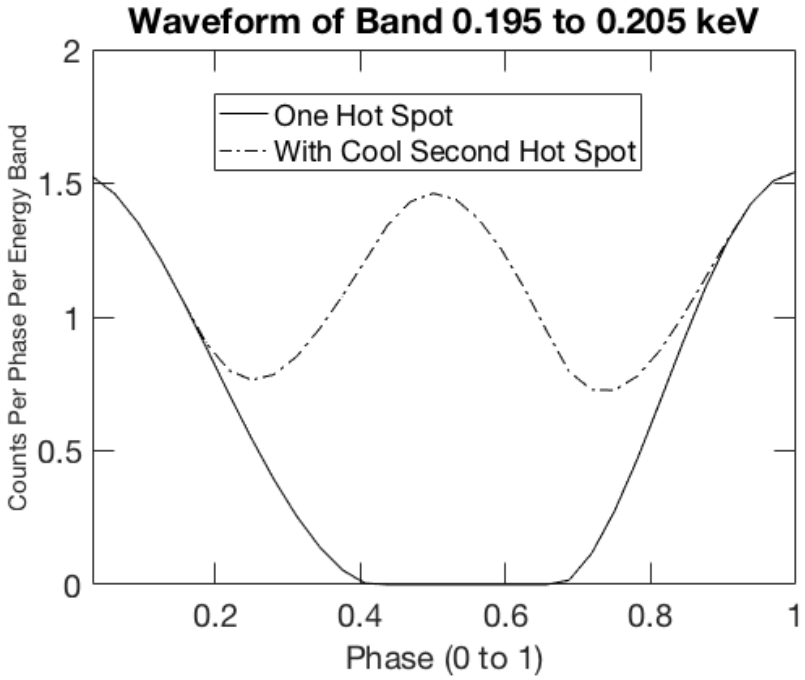

Figure 4.11: Contribution by the second spot is clearly seen in the soft energy bands

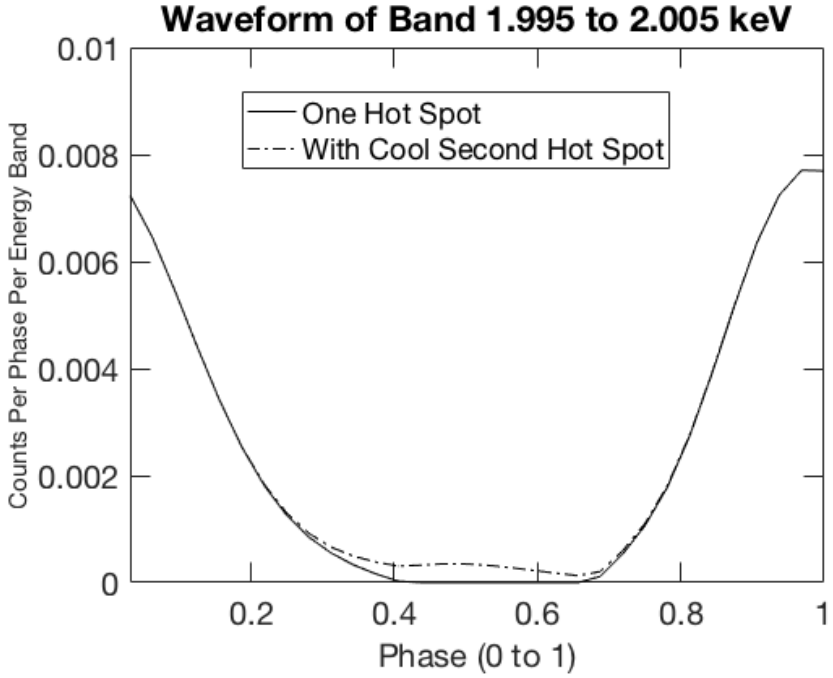

Figure 4.12: Contribution by the second spot diminishes at harder energy bands

4.2.6 Colatitude and Inclination Angles

The geometry of the spot and observer viewing angles also affects the resulting waveforms. The angle θ is the colatitude of the spot's centre, measured from the spin axis. The inclination angle, i, is the angle between the direction to the observer and the spin axis. See Figure 2.6 for the definition of these angles.

As an example, if we set the inclination to 50 degrees and colatitude angle to 70 degrees, the waveform never experiences an eclipse. The lack of eclipse for such orientation is demonstrated by Figure 4.13. Even though the hot spot is beyond the Newtonian horizon of $\psi = \pi/2$ for some time every phase, the favourable position of the hot spot and the compactness of the NS allow the light to be bent enough to be seen by the observer.

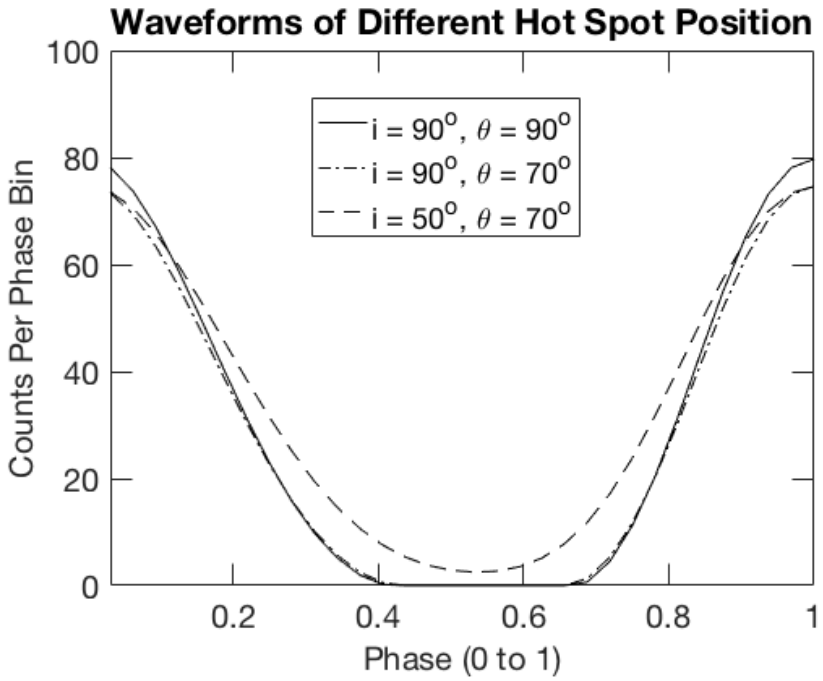

Figure 4.13: For $i = 50^o, \theta = 70^o$, no X-ray eclipse occurs even though the spot goes behind the Newtonian horizon momentarily.

4.2.7 Atmosphere Models

Here we examine the effect of the atmosphere on the NS light curve. Figure 4.14 shows the spectra of the light curves produced by using various atmosphere models. Applying the helium atmosphere model makes the spectrum harder than hydrogen model. This is a direct consequence of the harder intensity profile. The partially ionized hydrogen produces softer spectrum than the completely ionized model, due to the reduced hardening of the spectrum by Thomson scattering. The absorption lines are not visible at this surface temperature. McPHAC produces nearly identical light curve with the NSX version, as expected from the intensity profiles. Figure 4.15 shows the waveforms of the light curves produced by using various atmosphere models. There is essentially no difference in the shape of the waveforms, since the hot spot configurations are the same.

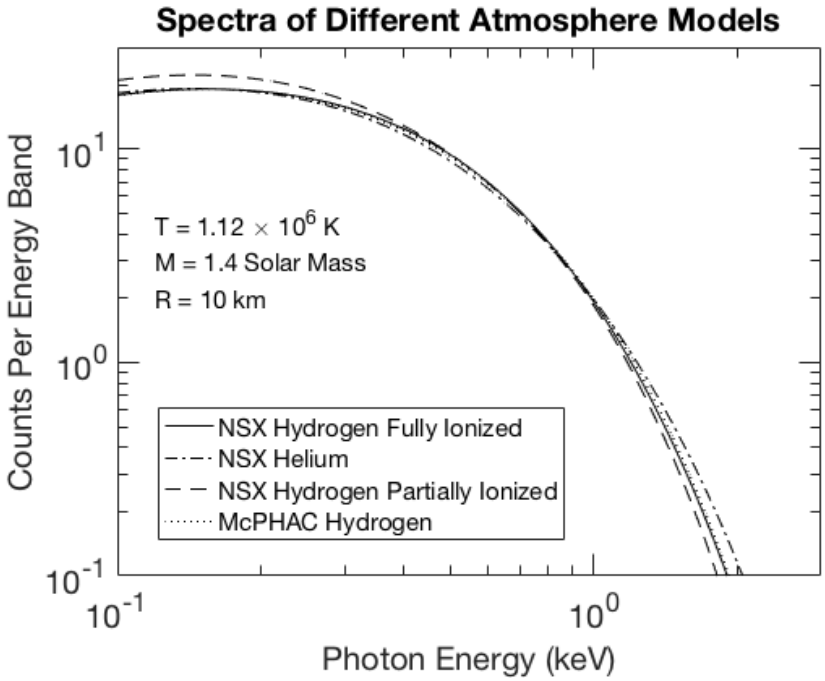

Figure 4.14: Properties of the atmosphere intensity profiles are present on the resulting spectra

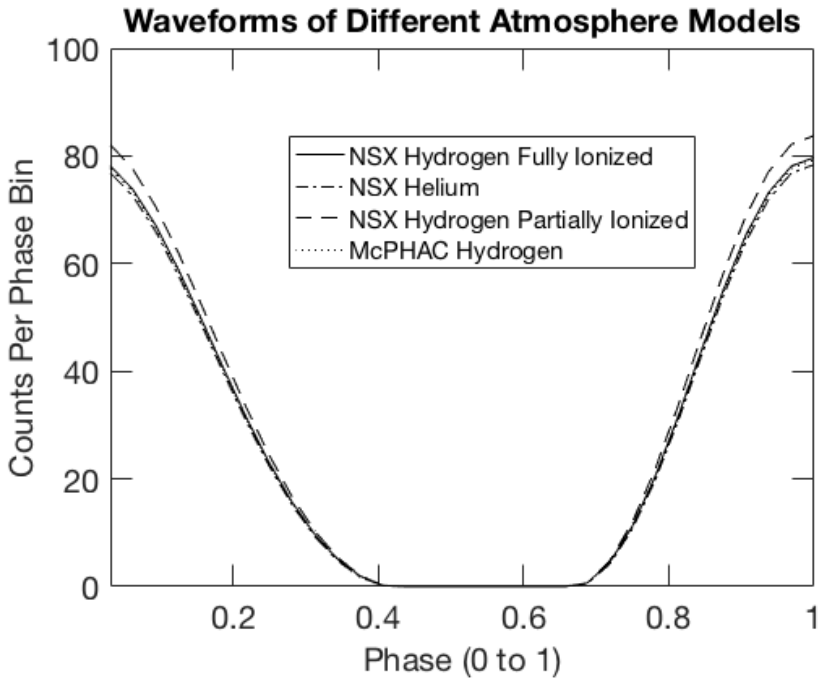

Figure 4.15: The general shape of the waveform remains the same with different atmosphere models.

4.2.8 ISM

Since the ISM absorbs soft X-ray more easily than hard X-ray, the amount of ISM in the line of sight greatly affects the number of soft X-ray photons observed. The ISM is opaque for visible light, but the absorptivity decreases for the photons with higher energies. We apply the *TBNew* ISM attenuation factors. Figure 4.16 shows the spectra produced using different values of hydrogen column density. The soft X-ray photon counts changes drastically, since the soft X-ray photons are more susceptible to ISM attenuation. Having a good estimate on the hydrogen column density could help constrain the hot spot temperature well, especially the cooler component of PSRJ0437.

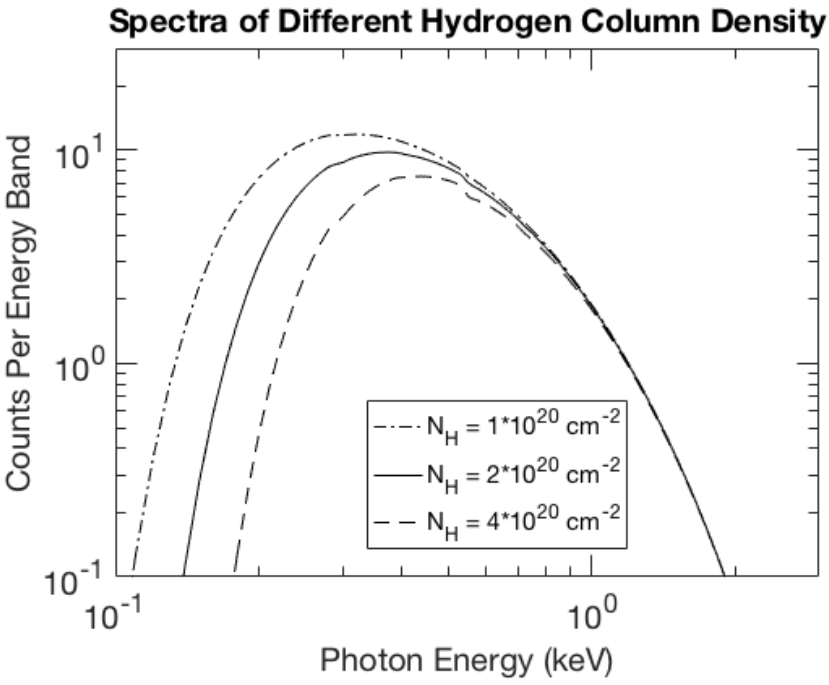

Figure 4.16: The amount of ISM determines how many soft X-ray photons arrive at the detector.

4.2.9 Redistribution by *NICER*'s Response Matrix

The response matrix of *NICER* determines how the photons are received. The photon signals are redistributed via the response matrix of *NICER*; photons are redistributed to a number of channels corresponding to energies around the true photon energy. The sharp peaks in the effective area curve are thus averaged-out to its nearby energy. Figure 4.17 shows the spectrum before and after the application of *NICER*'s response matrix. We normalize the spectrum to show the effect by the response matrix. The received photon flux spectrum peaks at 0.5 keV, instead of the inherent 0.3 keV. This is a combination of the NS inherent spectrum and *NICER*'s response matrix.

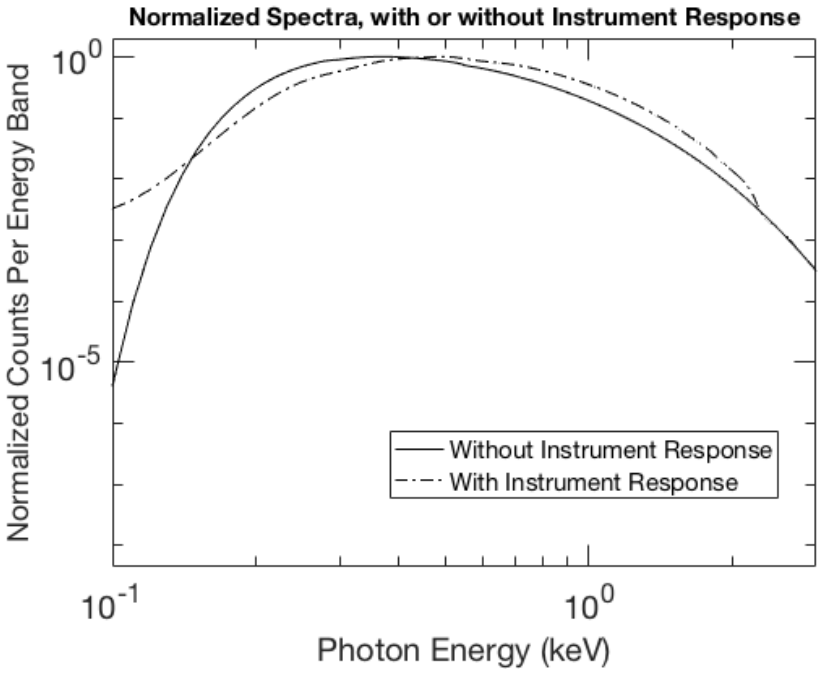

Figure 4.17: The spectrum's peak photon count is shifted to higher energy by *NICER*'s response matrix

4.3 Effects of NS Parameters: PSRJ0437

4.3.1 PSRJ0437 Statistics

Modelling the observation on PSRJ0437 sets the groundwork for making constraints on its mass-radius relation in the future. As described at the beginning of this chapter, we model the PSRJ0437 signal by using the NS properties previously constrained by Bogdanov et al. (2007), Bogdanov (2013), Reardon et al. (2016), and Deller et al. (2008). Bogdanov (2013) modelled the observation with hot spots of different sizes and temperatures, making its light curve dependent on both photon energy and waveform phase. First, we examine the properties of the spectrum at different phases and understand the contribution by each hot spot. Next, we examine the waveform properties at different energies. Finally, we calculate the difference in light curve with the application of alternative atmosphere models.

Previous efforts on PSRJ0437 established estimates and some measurements of its basic properties. We use the NSX hydrogen atmosphere model as default. Table 4.3 is the list of properties we use to model the observation. Estimates without citations were established by Bogdanov (2013), and measurements with radio data are cited in the table.

Parameter	Value
Mass	$1.44 M_{\odot}$ (Reardon et al., 2016)
Radius	13 km
Spin Frequency	173.6 Hz (Johnston et al., 1993)
Inclination Angle	42 degrees (0.733 radian) (Reardon et al., 2016)
Number of Hot Spots	2
Atmosphere Model	NSX hydrogen (fully-ionized)
Surface Temperature of Hot Spot 1	2.68×10^6 K
Angular Size of Hot Spot 1	0.013 radian
Emission Angle of Hot Spot 1	56 degrees (0.977 radian)
Surface Temperature of Hot Spot 2	6.71×10^5 K
Angular Size of Hot Spot 2	0.36 radian
Emission Angle of Hot Spot 2	131.78 degrees (2.3 radian)
Phase of Hot Spot 2	0.5625 cycle
Distance to NS	156.3 parsecs[2] (Deller et al., 2008)

Table 4.3: Best PSRJ0437 parameters from previous efforts. Estimates not labelled are established by Bogdanov (2013).

[2]We use NICER science team's suggestion of 156.3 parsecs, although there is a more recent measurement by Reardon et al. (2016).

We are modelling an observation by *NICER*, so background sources, the ISM, and the instrument response curve all contribute to the final signal:

Parameter	Value
Number of Energy Bands	301
Size of Energy Bands	0.01 keV
Energy Band Boundaries	0.095 to 3.105 keV
Observation Time	10^6 seconds
Background Contributions	AGN, Diffuse Sky
AGN Contribution	0.4 photons/second
Diffuse Sky Contribution	0.3 photons/second
ISM	*TBNew*
Hydrogen Column Density[3]	$2 * 10^{20} cm^{-2}$
Instrument Response Curve	*NICER* Response Curve

Table 4.4: Expected values in *NICER* observation on PSRJ0437

4.3.2 Spectral Evolution with Phase

We can learn about the energy of importance for the contributions from each component by examining the spectra at different phases. Figure 4.18 shows the modelled spectra of PSRJ0437 at two phases of importance. The two hot spots are face-on to the observer at phase 1 and 19, respectively. At energies below 0.12 keV, the spectra are nearly identical since the spectra is almost completely contributed by the diffuse sky; photons from the nearby AGN and PSRJ0437 are mostly absorbed by the ISM. At energies between 0.12 and 0.53 keV, the colder hot spot produces more flux than the warmer hot spot. The colder hot spot contributes more since it has a softer spectrum and a larger

[3]This is the N_H value reported by Bogdanov (2013) rounded to the nearest product of $4 * 10^{19} cm^{-2}$.

emission area. Several peaks caused by the effective area curve can be seen in the spectra, although they are smoothed by the redistribution matrix. At energies above 0.53 keV, the warmer hot spot has a greater contribution from its harder spectrum. The contribution from each hot spots can be clearly differentiated by examining the changing spectra for the phase bins.

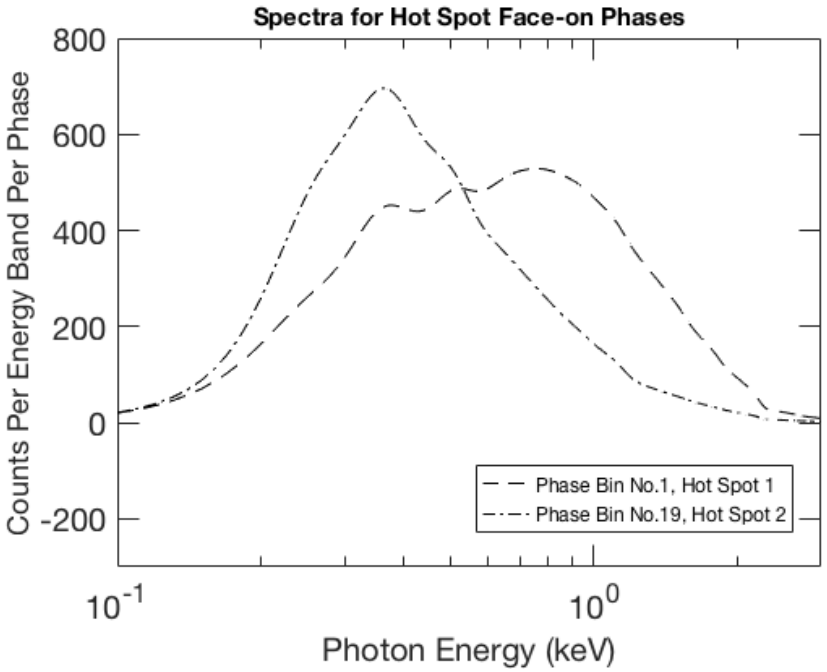

Figure 4.18: The contributions by the two hot spots are demonstrated with phase-specific spectra. The spectrum is harder when the hotter hot spot faces the observer.

4.3.3 Waveform Evolution with Photon Energy

Our interpretation of the contributions from each hot spot can be strengthened by examining the waveform at different photon energies. Figure 4.19 shows the waveform at 0.12 keV. The waveform is flat, meaning that there is no phase-dependent contribution from any of the hot spot.

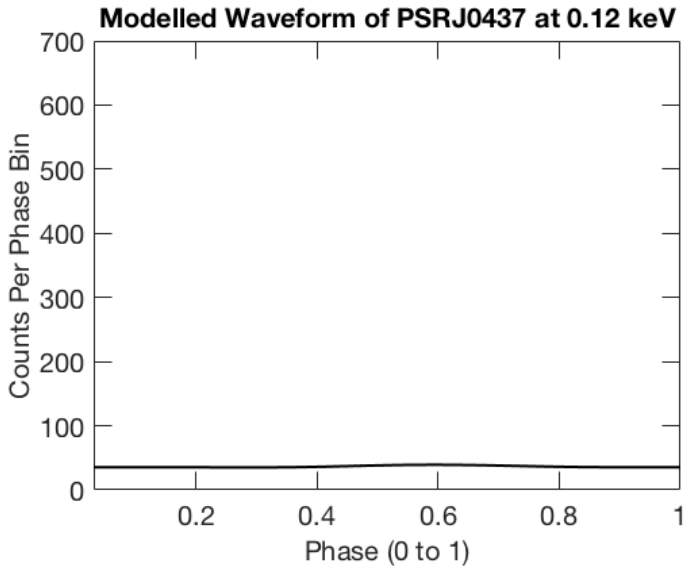

Figure 4.19: Waveform at 0.12 keV. No contribution by the hot spots are present.

Figure 4.20 shows the waveform at 0.36 keV. It has two peaks, with each corresponding to a hot spot. The colder hot spot, located near phase 0.6, has a greater contribution than the warmer hot spot. This energy band also has the most counts of all energy bands.

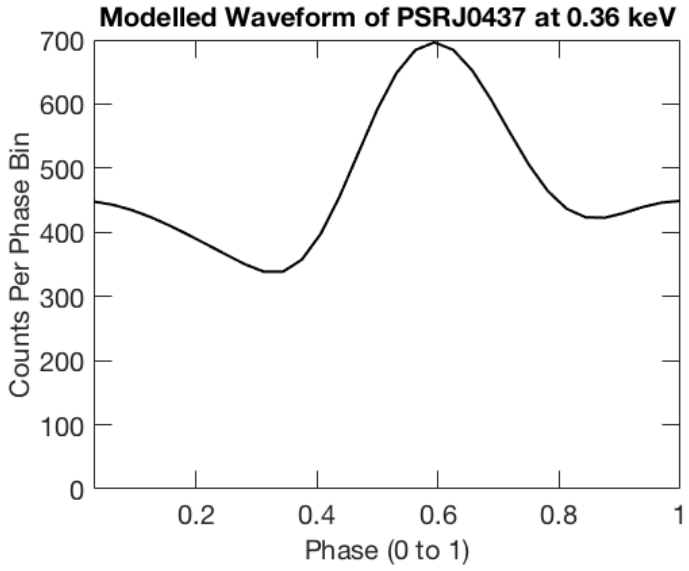

Figure 4.20: Waveform at 0.36 keV has the most counts of all energy bands.

Figure 4.21 shows the waveform at 0.53 keV. The two peaks are at same height, meaning that the contributions from the two spots are the same at this energy band.

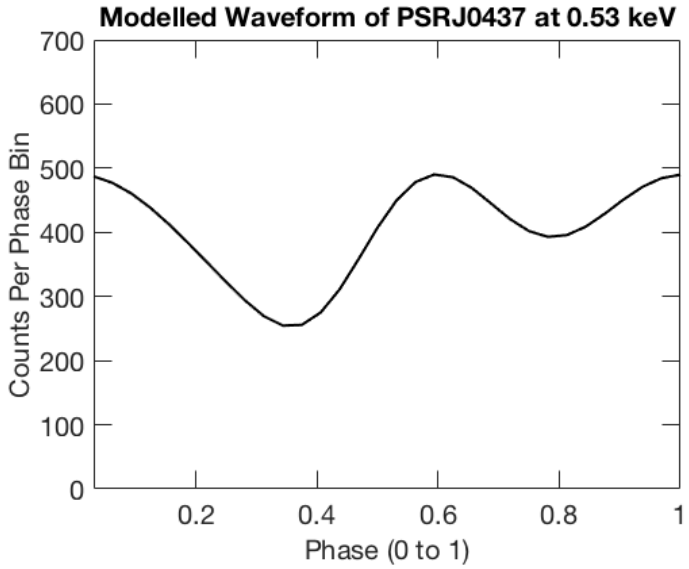

Figure 4.21: Waveform at 0.53 keV has equal contributions from the two hot spots.

Figure 4.22 shows the waveform at 1 keV. The second peak could barely be noticed at this energy band.

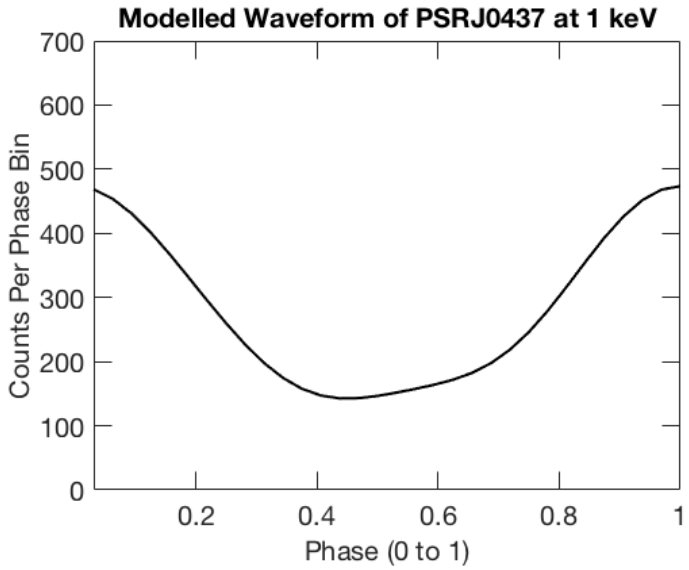

Figure 4.22: Waveform at 1.0 keV shows little contribution by the colder hot spot.

Figure 4.23 shows the waveform at 2.23 keV. The total number of photons observed is only 5% of the number of photons at 0.36 keV.

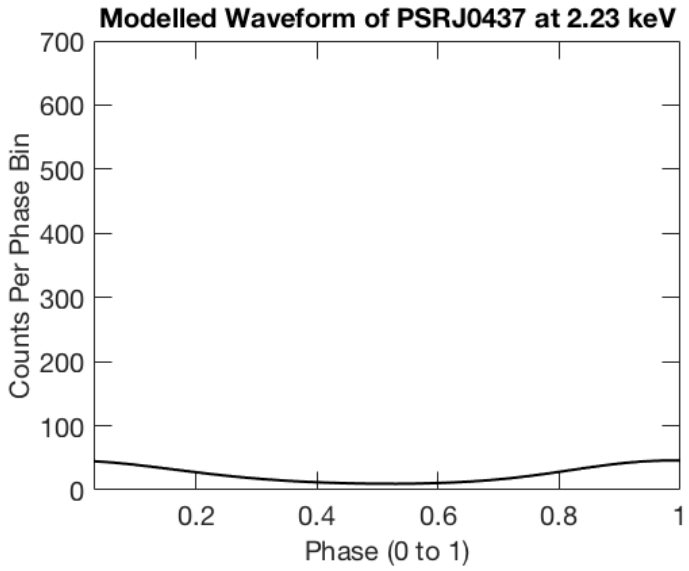

Figure 4.23: The total number of photons observed at 2.23 keV is only 5% of the number of photons at 0.36 keV.

This is the combined result between the high-energy tail of the NS atmosphere intensity profile and the insensitivity of *NICER* instrument towards

harder X-ray photons. The phase-dependent power-law tail not modelled in this project is expected to have a greater contribution than the hot spots at 3 keV (Guillot et al., 2016). However, we estimate less than 200 photons per energy band are contributed by the hot spots above this energy, which means that the power-law tail should have small contribution in the overall light curve. The contribution from each hot spot is clearly seen in the waveforms at different energy, further supports the interpretation from the spectral analysis.

4.3.4 Comparison of Alternative Atmosphere Models

We verify the validity of NSX hydrogen atmosphere model by comparing the resultant light curve with other atmosphere models. Figure 4.24 shows the modelled phase-summed spectra of McPHAC and NSX Hydrogen models. The McPHAC Hydrogen model produces nearly identical spectra with NSX hydrogen. Since they are constructed independently, this shows that both models capture the nature of NS hydrogen atmosphere quite well.

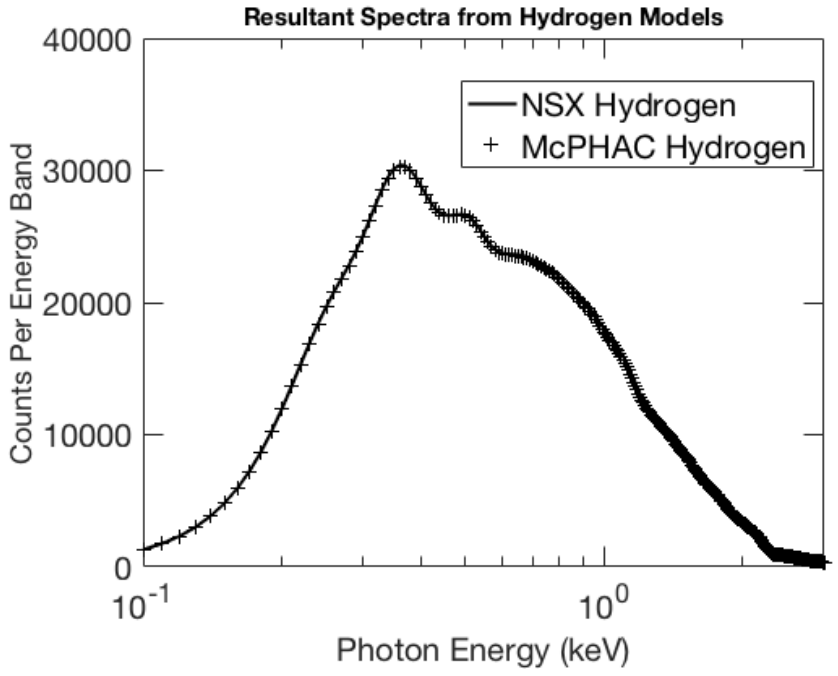

Figure 4.24: The spectrum produced by McPHAC Hydrogen model agrees very well with NSX Hydrogen model

Figure 4.25 shows the modelled phase-summed spectra of NSX Hydrogen and NSX Helium models. The photon counts between 0.1 and 1.5 keV for NSX Helium model is lower than the NSX Hydrogen counterpart. This is expected from the weaker peak of the helium intensity profile. Even though the helium model produces a harder high-energy tail, it is less obvious in the resultant spectra due to the insensitivity of *NICER* instrument at higher energies. The light curve from NSX helium model may not be applicable to PSRJ0437 since it is unlikely to have a helium surface, but the helium model would be important should new discoveries X-ray millisecond pulsars in ultra-compact X-ray binary arise.

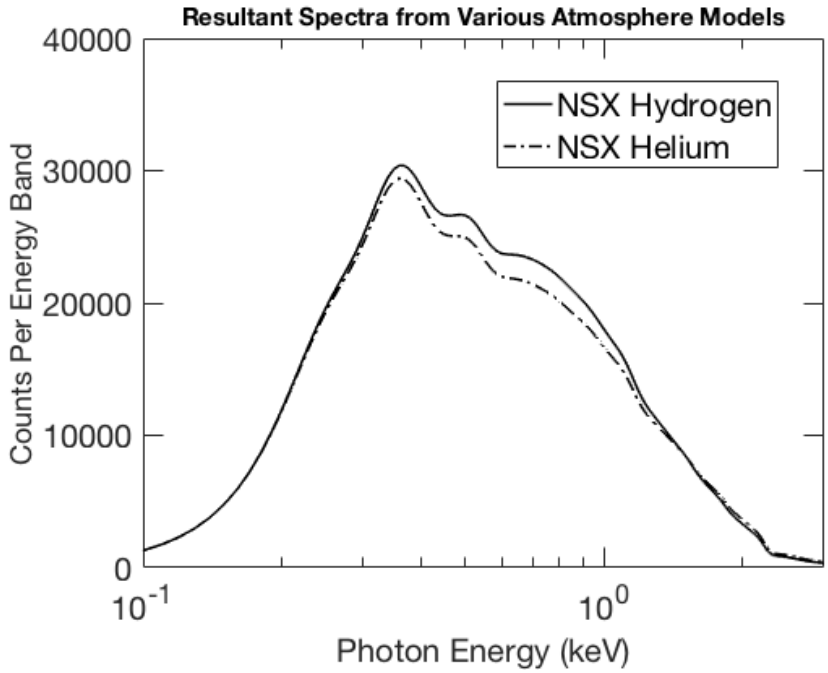

Figure 4.25: Compared to hydrogen, helium atmosphere produces less counts between 0.1 and 1.5 keV and slightly more counts above 1.5 keV.

4.4 Chapter Summary

We have investigated the properties of the light curve modelling program in this chapter. By using two toy models, we are able to see how the neutron

star parameters influence light curves. The neutron star parameters can be roughly categorized into light curve settings, neutron star configuration, and signal processing. The neutron star parameters influence the light curve by general-relativistic effects such as Doppler boost and bending of light. The spectra are influenced by the amount of ISM and the response curve of the NICER telescope. Last but not least, the modelled light curves are influenced by the choice of atmosphere models and their emergent intensity profiles. The properties of the light curves can be clearly seen with our two models.

Chapter 5

Conclusion

Constraining the mass-radius relation provides a potential answer to the currently uncertain equation of state of cold dense matter. The interior of neutron stars contains matter at extremely high pressure and density conditions. The current equation of state at such densities is uncertain, since experiments to replicate the condition is impossible with current technologies. Using the equation of hydrostatic equilibrium, the candidate equations of state can be used to predict mass-radius curves for neutron stars. Obtaining highly-constrained neutron star masses and radii thus verifies the validity of competing equations of state.

The properties of rotation-powered X-ray millisecond pulsars allows for potential measurements of highly-constrained neutron star masses and radii. The X-ray modulation from rotation-powered X-ray millisecond pulsars are caused by their surface hot spots. The light curves from such objects are sensitive to changes in both mass and radius, allowing simultaneous constraints to be put on them. Efforts in hot spot modelling, emergent thermal spectra from surface atmosphere, and improved spectral and timing capabilities for X-ray telescopes are in place to put more stringent constraints on the properties of rotation-powered X-ray millisecond pulsars.

Neutron star atmosphere models are required to obtain accurate flux that

reflects the properties of the non-accreting neutron stars. We examine the intensity profiles from the candidate neutron star atmosphere models. To obtain small interpolation error, we establish that the general algorithm should follow the power-law scheme, which is a direct result from the thermal nature of the atmosphere. In particular, two-point interpolation can be used for temperature, surface gravity, and emission angle to surface normal, while photon energy requires four-point interpolation. The strong temperature dependence is seen clearly between the intensity profiles at different temperature, while helium produces overall flatter profiles than hydrogen due to the stronger Thomson scattering.

The light curve model encapsulates the many physical effects created by neutron stars, surrounding background sources, interstellar medium, and X-ray telescopes. By applying the atmosphere models to the hot spot model, we examine the effects of neutron star parameters on the light curve. The fast-spinning neutron star causes the waveform to deform due to the changed times of arrival as well as the hardening of the spectrum by Doppler shift. The compact nature of the neutron star increase the light-bending, allowing the hot spot to be visible beyond the Newtonian horizon, and the photons experience strong gravitational redshift. The light curve is heavily influenced by temperature, with its effect seen across spectra and waveforms. The amount of ISM determines the contributions by the soft X-ray, since they are attenuated more easily by ISM. The instrument response curve also plays a role in the contribution by photons with different energies, since *NICER* telescope has a changing sensitivity across the soft X-ray band.

PSR J0437-4715 is the closest rotation-powered X-ray millisecond pulsar, making it the ideal candidate to apply the light curve method in constraining the mass-radius relation for neutron stars. We apply high-accuracy atmosphere models of McPHAC hydrogen, NSX hydrogen, and NSX helium to neutron star hot spot model. Combining with realistic background, ISM attenuation, and

NICER instrumental response, we created light curves with both spectral and timing properties. The properties of the two hot spots at different temperature is best demonstrated by using both its spectra and waveforms, strengthening the need for the spectral and timing capabilities in which *NICER* will provide.

Future work will aim at improving the applicability of this project. First, improving the reliability, efficiency, and accuracy of the current code allows for greater exploitation of the neutron star light curve method. Next, working with a wider variety of the atmosphere models such as the partially-ionized hydrogen or other surface compositions such as oxygen or carbon would allow for a wider range of the neutron stars to be modelled. Finally, applying the current work with a fitting routine could put constrain on the mass-radius relation of neutron stars with future observation of *NICER* on PSR J0437-4715. This can be done with Monte Carlo-Markov Chain as previously done by Miller and Lamb (2015) and Lo et al. (2013) or genetic evolution method as previously done by Stevens et al. (2016).

Bibliography

M. AlGendy and S. M. Morsink. Universality of the Acceleration due to Gravity on the Surface of a Rapidly Rotating Neutron Star. *The Astrophysical Journal*, 791:78, August 2014. doi: 10.1088/0004-637X/791/2/78.

M. A. Alpar, A. F. Cheng, M. A. Ruderman, and J. Shaham. A new class of radio pulsars. *Nature*, 300:728–730, December 1982. doi: 10.1038/300728a0.

E. Anders and N. Grevesse. Abundances of the elements - Meteoritic and solar. *Geochimica et Cosmochimica Acta*, 53:197–214, January 1989. doi: 10.1016/0016-7037(89)90286-X.

Z. Arzoumanian, K. C. Gendreau, C. L. Baker, T. Cazeau, P. Hestnes, J. W. Kellogg, S. J. Kenyon, R. P. Kozon, K.-C. Liu, S. S. Manthripragada, C. B. Markwardt, A. L. Mitchell, J. W. Mitchell, C. A. Monroe, T. Okajima, S. E. Pollard, D. F. Powers, B. J. Savadkin, L. B. Winternitz, P. T. Chen, M. R. Wright, R. Foster, G. Prigozhin, R. Remillard, and J. Doty. The neutron star interior composition explorer (NICER): mission definition. In *Society of Photo-Optical Instrumentation Engineers (SPIE) Conference Series*, volume 9144 of *Society of Photo-Optical Instrumentation Engineers (SPIE) Conference Series*, page 20, July 2014. doi: 10.1117/12.2056811.

W. Baade and F. Zwicky. Remarks on Super-Novae and Cosmic Rays. *Physical Review*, 46:76–77, July 1934. doi: 10.1103/PhysRev.46.76.2.

M. Bauböck, F. Özel, D. Psaltis, and S. M. Morsink. Rotational Corrections to

Neutron-star Radius Measurements from Thermal Spectra. *The Astrophysical Journal*, 799:22, January 2015. doi: 10.1088/0004-637X/799/1/22.

S. Bogdanov. The Nearest Millisecond Pulsar Revisited with XMM-Newton: Improved Mass-radius Constraints for PSR J0437-4715. *The Astrophysical Journal*, 762:96, January 2013. doi: 10.1088/0004-637X/762/2/96.

S. Bogdanov, G. B. Rybicki, and J. E. Grindlay. Constraints on Neutron Star Properties from X-Ray Observations of Millisecond Pulsars. *The Astrophysical Journal*, 670:668–676, November 2007. doi: 10.1086/520793.

E. F. Brown, L. Bildsten, and R. E. Rutledge. Crustal Heating and Quiescent Emission from Transiently Accreting Neutron Stars. *The Astrophysical Journal*, 504:L95–L98, September 1998. doi: 10.1086/311578.

C. Cadeau. *Implications of Rapid Rotation for Pulse Profile Models of Millisecond-period X-ray Pulsars*. PhD thesis, University of Alberta, 2007.

C. Cadeau, S. M. Morsink, D. Leahy, and S. S. Campbell. Light Curves for Rapidly Rotating Neutron Stars. *The Astrophysical Journal*, 654:458–469, January 2007. doi: 10.1086/509103.

B. W. Carroll and D. A. Ostlie. *An Introduction to Modern Astrophysics*. Addison-Wesley, 2007.

A. Cumming. Lecture notes for CRAQ Summer School on Compact Objects at McGill University, August 2016.

A. T. Deller, J. P. W. Verbiest, S. J. Tingay, and M. Bailes. Extremely High Precision VLBI Astrometry of PSR J0437-4715 and Implications for Theories of Gravity. *The Astrophysical Journal Letters*, 685:L67, September 2008. doi: 10.1086/592401.

K. G. Elshamouty. *Characteristics of Neutron Stars from X-Rays Observations*. PhD thesis, University of Alberta, 2016.

K. G. Elshamouty, C. O. Heinke, S. M. Morsink, S. Bogdanov, and A. L. Stevens. The Impact of Surface Temperature Inhomogeneities on Quiescent Neutron Star Radius Measurements. *The Astrophysical Journal*, 826:162, August 2016. doi: 10.3847/0004-637X/826/2/162.

M. Feroci, J. W. den Herder, E. Bozzo, D. Barret, S. Brandt, M. Hernanz, M. van der Klis, M. Pohl, A. Santangelo, L. Stella, and et al. LOFT: the Large Observatory For X-ray Timing. In *Space Telescopes and Instrumentation 2012: Ultraviolet to Gamma Ray*, volume 8443 of *Proceedings of SPIE*, page 84432D, September 2012. doi: 10.1117/12.926310.

S. Guillot, V. M. Kaspi, R. F. Archibald, M. Bachetti, C. Flynn, F. Jankowski, M. Bailes, S. Boggs, F. E. Christensen, W. W. Craig, C. A. Hailey, F. A. Harrison, D. Stern, and W. W. Zhang. The NuSTAR view of the non-thermal emission from PSR J0437-4715. *Monthly Notices of the Royal Astronomical Society*, 463:2612–2622, December 2016. doi: 10.1093/mnras/stw2194.

C. B. Haakonsen, M. L. Turner, N. A. Tacik, and R. E. Rutledge. The McGill Planar Hydrogen Atmosphere Code (McPHAC). *The Astrophysical Journal*, 749:52, April 2012. doi: 10.1088/0004-637X/749/1/52.

C. O. Heinke, G. B. Rybicki, R. Narayan, and J. E. Grindlay. A Hydrogen Atmosphere Spectral Model Applied to the Neutron Star X7 in the Globular Cluster 47 Tucanae. *The Astrophysical Journal*, 644:1090–1103, June 2006. doi: 10.1086/503701.

J. W. T. Hessels, S. M. Ransom, I. H. Stairs, P. C. C. Freire, V. M. Kaspi, and F. Camilo. A Radio Pulsar Spinning at 716 Hz. *Science*, 311:1901–1904, March 2006. doi: 10.1126/science.1123430.

A. Hewish, S. J. Bell, J. D. H. Pilkington, P. F. Scott, and R. A. Collins. Observation of a Rapidly Pulsating Radio Source. *Nature*, 217:709–713, February 1968. doi: 10.1038/217709a0.

W. C. G. Ho. private communication, 2017.

W. C. G. Ho and C. O. Heinke. A neutron star with a carbon atmosphere in the Cassiopeia A supernova remnant. *Nature*, 462:71–73, November 2009. doi: 10.1038/nature08525.

W. F. Huebner, A. L. Mertz, N. H. Jr. Magee, and M F. Argo. Los Alamos Report LA-6760-M. Technical report, Astrophysical Opacity Library, 1977.

C. A. Iglesias, F. J. Rogers, and B. G. Wilson. Reexamination of the metal contribution to astrophysical opacity. *The Astrophysical Journal Letters*, 322:L45–L48, November 1987. doi: 10.1086/185034.

T. J. Johnson, C. Venter, A. K. Harding, L. Guillemot, D. A. Smith, M. Kramer, Ö. Çelik, P. R. den Hartog, E. C. Ferrara, X. Hou, J. Lande, and P. S. Ray. Constraints on the Emission Geometries and Spin Evolution of Gamma-Ray Millisecond Pulsars. *The Astrophysical Journal Supplement*, 213:6, July 2014. doi: 10.1088/0067-0049/213/1/6.

S. Johnston, D. R. Lorimer, P. A. Harrison, M. Bailes, A. G. Lyne, J. F. Bell, V. M. Kaspi, R. N. Manchester, N. D'Amico, and L. Nicastro. Discovery of a very bright, nearby binary millisecond pulsar. *Nature*, 361:613–615, February 1993. doi: 10.1038/361613a0.

J. M. Lattimer and A. W. Steiner. Neutron Star Masses and Radii from Quiescent Low-mass X-Ray Binaries. *The Astrophysical Journal*, 784:123, April 2014. doi: 10.1088/0004-637X/784/2/123.

W. H. G. Lewin, J. V. Paradijs, and R. E. Taam. X-ray bursts. In *X-Ray Binaries*. Cambridge Astrophysics Series, 1995.

K. H. Lo, M. C. Miller, S. Bhattacharyya, and F. K. Lamb. Determining Neutron Star Masses and Radii Using Energy-resolved Waveforms of X-Ray

Burst Oscillations. *The Astrophysical Journal*, 776:19, October 2013. doi: 10.1088/0004-637X/776/1/19.

D. Lorimer and M. Kramer. *Handbook of Pulsar Astronomy*. Cambridge University Press, 2005.

J. E. McClintock, R. Narayan, and G. B. Rybicki. On the Lack of Thermal Emission from the Quiescent Black Hole XTE J1118+480: Evidence for the Event Horizon. *The Astrophysical Journal*, 615:402–415, November 2004. doi: 10.1086/424474.

M. C. Miller and F. K. Lamb. Bounds on the Compactness of Neutron Stars from Brightness Oscillations during X-Ray Bursts. *The Astrophysical Journal*, 499:L37–L40, May 1998. doi: 10.1086/311335.

M. C. Miller and F. K. Lamb. Determining Neutron Star Properties by Fitting Oblate-star Waveform Models to X-Ray Burst Oscillations. *The Astrophysical Journal*, 808:31, July 2015. doi: 10.1088/0004-637X/808/1/31.

S. M. Morsink, D. A. Leahy, C. Cadeau, and J. Braga. The Oblate Schwarzschild Approximation for Light Curves of Rapidly Rotating Neutron Stars. *The Astrophysical Journal*, 663:1244–1251, July 2007. doi: 10.1086/518648.

G. Nelemans, P. G. Jonker, and D. Steeghs. Optical spectroscopy of (candidate) ultracompact X-ray binaries: constraints on the composition of the donor stars. *Monthly Notices of the Royal Astronomical Society*, 370:255–262, July 2006. doi: 10.1111/j.1365-2966.2006.10496.x.

S. Olausen. Light curves of very compact neutron stars. Master's thesis, University of Alberta, 2008.

S. A. Olausen and V. M. Kaspi. The McGill Magnetar Catalog. *The Astrophysical Journal*, 212:6, May 2014. doi: 10.1088/0067-0049/212/1/6.

J. R. Oppenheimer and G. M. Volkoff. On Massive Neutron Cores. *Physical Review*, 55:374–381, February 1939. doi: 10.1103/PhysRev.55.374.

K. R. Pechenick, C. Ftaclas, and J. M. Cohen. Hot spots on neutron stars - The near-field gravitational lens. *The Astrophysical Journal*, 274:846–857, November 1983. doi: 10.1086/161498.

J. Poutanen and M. Gierliński. On the nature of the X-ray emission from the accreting millisecond pulsar SAX J1808.4-3658. *Monthly Notices of the Royal Astronomical Society*, 343:1301–1311, August 2003. doi: 10.1046/j.1365-8711.2003.06773.x.

W. H. Press, S. A. Teukolsky, W. T. Vetterling, and B. P. Flannery. *Numerical Recipes*. Cambridge University Press, 2007.

M. Rajagopal and R. W. Romani. Model Atmospheres for Low-Field Neutron Stars. *The Astrophysical Journal*, 461:327, April 1996. doi: 10.1086/177059.

S. M. Ransom, J. W. T. Hessels, I. H. Stairs, P. C. C. Freire, F. Camilo, V. M. Kaspi, and D. L. Kaplan. Twenty-One Millisecond Pulsars in Terzan 5 Using the Green Bank Telescope. *Science*, 307:892–896, February 2005. doi: 10.1126/science.1108632.

D. J. Reardon, G. Hobbs, W. Coles, Y. Levin, M. J. Keith, M. Bailes, N. D. R. Bhat, S. Burke-Spolaor, S. Dai, M. Kerr, P. D. Lasky, R. N. Manchester, S. Osłowski, V. Ravi, R. M. Shannon, W. van Straten, L. Toomey, J. Wang, L. Wen, X. P. You, and X.-J. Zhu. Timing analysis for 20 millisecond pulsars in the Parkes Pulsar Timing Array. *Monthly Notices of the Royal Astronomical Society*, 455:1751–1769, January 2016. doi: 10.1093/mnras/stv2395.

R. W. Romani. Model atmospheres for cooling neutron stars. *The Astrophysical Journal*, 313:718–726, February 1987. doi: 10.1086/165010.

G. B. Rybicki. A modified Feautrier method. *Journal of Quantitative Spectroscopy and Radiative Transfer*, 11:589–595, 1971. doi: 10.1016/0022-4073(71)90040-9.

G. B. Rybicki and A. P. Lightman. *Radiative Processes in Astrophysics*. Wiley-Interscience, 1979.

S. L. Shapiro and S. A. Teukolsky. *Black Holes, White Dwarfs, and Neutron Stars*. Wiley-Interscience, 1983.

N. Shibazaki, T. Murakami, J. Shaham, and K. Nomoto. Does mass accretion lead to field decay in neutron stars? *Nature*, 342:656–658, December 1989. doi: 10.1038/342656a0.

K. P. Singh, S. N. Tandon, P. C. Agrawal, H. M. Antia, R. K. Manchanda, J. S. Yadav, S. Seetha, M. C. Ramadevi, A. R. Rao, D. Bhattacharya, B. Paul, P. Sreekumar, S. Bhattacharyya, G. C. Stewart, J. Hutchings, S. A. Annapurni, S. K. Ghosh, J. Murthy, A. Pati, N. K. Rao, C. S. Stalin, V. Girish, K. Sankarasubramanian, S. Vadawale, V. B. Bhalerao, G. C. Dewangan, D. K. Dedhia, M. K. Hingar, T. B. Katoch, A. T. Kothare, I. Mirza, K. Mukerjee, H. Shah, P. Shah, R. Mohan, A. K. Sangal, S. Nagabhusana, S. Sriram, J. P. Malkar, S. Sreekumar, A. F. Abbey, G. M. Hansford, A. P. Beardmore, M. R. Sharma, S. Murthy, R. Kulkarni, G. Meena, V. C. Babu, and J. Postma. ASTROSAT mission. In *Society of Photo-Optical Instrumentation Engineers (SPIE) Conference Series*, volume 9144 of *Society of Photo-Optical Instrumentation Engineers (SPIE) Conference Series*, page 1, July 2014. doi: 10.1117/12.2062667.

N. Stergioulas and J. L. Friedman. Comparing models of rapidly rotating relativistic stars constructed by two numerical methods. *The Astrophysical Journal*, 444:306–311, May 1995. doi: 10.1086/175605.

A. L. Stevens. Understanding parameter degeneracies in neutron star x-ray light curves. Master's thesis, University of Alberta, 2013.

A. L. Stevens, J. D. Fiege, D. A. Leahy, and S. M. Morsink. Neutron Star Mass-Radius Constraints Using Evolutionary Optimization. *The Astrophysical Journal*, 833:244, December 2016. doi: 10.3847/1538-4357/833/2/244.

T. Wang, C. Otani, M. Matsuoka, M. Cappi, K. M. Leighly, and W. Brinkmann. ASCA and ROSAT observations of the Seyfert 1 galaxy RX J0437.4-4711. *Monthly Notices of the Royal Astronomical Society*, 293: 397, February 1998. doi: 10.1046/j.1365-8711.1998.01135.x.

A. L. Watts, N. Andersson, D. Chakrabarty, M. Feroci, K. Hebeler, G. Israel, F. K. Lamb, M. C. Miller, S. Morsink, F. Özel, A. Patruno, J. Poutanen, D. Psaltis, A. Schwenk, A. W. Steiner, L. Stella, L. Tolos, and M. van der Klis. Colloquium: Measuring the neutron star equation of state using x-ray timing. *Reviews of Modern Physics*, 88(2):021001, April 2016. doi: 10.1103/RevModPhys.88.021001.

N. E. White, F. Nagase, and A. N. Oarmar. The properties of x-ray binaries. In *X-Ray Binaries*. Cambridge Astrophysics Series, 1995.

J. Wilms, A. Allen, and R. McCray. On the Absorption of X-Rays in the Interstellar Medium. *The Astrophysical Journal*, 542:914–924, October 2000. doi: 10.1086/317016.

C. A. Wilson-Hodge, P. S. Ray, K. Gendreau, D. Chakrabarty, M. Feroci, T. Maccarone, Z. Arzoumanian, R. A. Remillard, K. Wood, C. Griffith, and STROBE-X Collaboration. STROBE-X: X-ray Timing & Spectroscopy on Dynamical Timescales from Microseconds to Years. In *American Astronomical Society Meeting Abstracts*, volume 229 of *American Astronomical Society Meeting Abstracts*, page 309.04, January 2017.

V. E. Zavlin, G. G. Pavlov, and Y. A. Shibanov. Model neutron star atmospheres with low magnetic fields. I. Atmospheres in radiative equilibrium. *Astronomy and Astrophysics*, 315:141–152, November 1996.

S. N. Zhang, M. Feroci, A. Santangelo, Y. W. Dong, H. Feng, F. J. Lu, K. Nandra, Z. S. Wang, S. Zhang, E. Bozzo, S. Brandt, A. De Rosa, L. J. Gou, M. Hernanz, M. van der Klis, X. D. Li, Y. Liu, P. Orleanski, G. Pareschi, M. Pohl, J. Poutanen, J. L. Qu, S. Schanne, L. Stella, P. Uttley, A. Watts, R. X. Xu, W. F. Yu, J. J. M. in 't Zand, S. Zane, L. Alvarez, L. Amati, L. Baldini, C. Bambi, S. Basso, Bhattacharyya S., B. , R., T. Belloni, P. Bellutti, S. Bianchi, A. Brez, M. Bursa, V. Burwitz, C. Budtz-Jørgensen, I. Caiazzo, R. Campana, X. Cao, P. Casella, C. Y. Chen, L. Chen, T. Chen, Y. Chen, Y. Chen, Y. P. Chen, M. Civitani, F. Coti Zelati, W. Cui, W. W. Cui, Z. G. Dai, E. Del Monte, D. de Martino, S. Di Cosimo, S. Diebold, M. Dovciak, I. Donnarumma, V. Doroshenko, P. Esposito, Y. Evangelista, Y. Favre, P. Friedrich, F. Fuschino, J. L. Galvez, Z. L. Gao, M. Y. Ge, O. Gevin, D. Goetz, D. W. Han, J. Heyl, J. Horak, W. Hu, F. Huang, Q. S. Huang, R. Hudec, D. Huppenkothen, G. L. Israel, A. Ingram, V. Karas, D. Karelin, P. A. Jenke, L. Ji, S. Korpela, D. Kunneriath, C. Labanti, G. Li, X. Li, Z. S. Li, E. W. Liang, O. Limousin, L. Lin, Z. X. Ling, H. B. Liu, H. W. Liu, Z. Liu, B. Lu, N. Lund, D. Lai, B. Luo, T. Luo, B. Ma, S. Mahmoodifar, M. Marisaldi, A. Martindale, N. Meidinger, Y. Men, M. Michalska, R. Mignani, M. Minuti, S. Motta, F. Muleri, J. Neilsen, M. Orlandini, A. T. Pan, A. Patruno, E. Perinati, A. Picciotto, C. Piemonte, M. Pinchera, Rachevski A., M. Rapisarda, N. Rea, E. M. R. Rossi, A. Rubini, G. Sala, X. W. Shu, C. Sgro, Z. X. Shen, P. Soffitta, L. Song, G. Spandre, G. Stratta, T. E. Strohmayer, L. Sun, J. Svoboda, G. Tagliaferri, G. Tenzer, T. Hong, R. Taverna, G. Torok, R. Turolla, S. Vacchi, J. Wang, D. Walton, K. Wang, J. F. Wang, R. J. Wang, Y. F. Wang, S. S. Weng, J. Wilms, B. Winter, X. Wu, X. F. Wu, S. L. Xiong, Y. P. Xu, Y. Q. Xue, Z. Yan, S. Yang, X. Yang, Y. J.

Yang, F. Yuan, W. M. Yuan, Y. F. Yuan, G. Zampa, N. Zampa, A. Zdziarski, C. Zhang, C. L. Zhang, L. Zhang, X. Zhang, Z. Zhang, W. D. Zhang, S. J. Zheng, P. Zhou, and Zhou X. L. eXTP: Enhanced X-ray Timing and Polarization mission. In *Space Telescopes and Instrumentation 2016: Ultraviolet to Gamma Ray*, volume 9905 of *Proceedings of SPIE*, page 99051Q, July 2016. doi: 10.1117/12.2232034.